Journal of the Mechanics and Physics of Solids 133 (2019) 103734

Contents lists available at ScienceDirect

Journal of the Mechanics and Physics of Solids

journal homepage: www.elsevier.com/locate/jmps

Wrinkling to crinkling transitions and curvature localization in a magnetoelastic film bonded to a non-magnetic substrate

E. Psarra, L. Bodelot, K. Danas*

LMS, C.N.R.S, École Polytechnique, Institut Polytechnique de Paris, Palaiseau, 91128, France

ARTICLE INFO

Article history:
Received 3 July 2019
Revised 25 August 2019
Accepted 14 September 2019
Available online 15 September 2019

Keywords:
Magnetorheological elastomers
Magnetoelasticity
Film-substrate wrinkling
Bifurcation
Surface patterns
Curvature localization
Crinkling

ABSTRACT

This work studies experimentally and numerically the post-bifurcation response of a magnetorheological elastomer (MRE) film bonded to a soft non-magnetic (passive) substrate. The film-substrate system is subjected to a combination of an axial mechanical pre-compression and a transverse magnetic field. The non-trivial interaction of the two fields leads to a decrease of the critical magnetic field with applied pre-compression, while the observed wrinkling patterns evolve into crinkles, a bifurcation mode that is defined by the accompanied curvature localization and strong shearing of the side faces of the wrinkled geometry. Using a magneto-elastic variational formulation in a two-dimensional finite element numerical setting, we find that the crinkling is an intrinsic feature of magnetoelasticity and its presence is directly associated with the repulsive magnetic forces of the neighboring wrinkled-crinkled faces. As a result, the presence of the magnetic field prohibits the formation of creases and folds. In an effort to obtain a good quantitative agreement between the numerical and the experimental results, we also introduce an approximate way to model the friction of the lateral film-substrate faces. This analysis reveals the strong effects of friction upon the magneto-mechanical wrinkling modes.

1. Introduction

Mechanically stiff films bonded on passive compliant substrates are known to undergo mechanical instabilities under uniaxial compressive loads (Bowden et al., 1998; Huang, 2005). The principal solution of such material systems is unique and stable until the load exceeds a critical value, which then causes the film to bifurcate into a wrinkled deformation mode. The critical bifurcation load and wavelength of the patterns is directly influenced by the contrast of the properties between the film and the substrate (Hutchinson, 2013; Jin and Suo, 2015; Kim et al., 2011; Sun et al., 2012). In the post-bifurcation regime and for significant mechanical contrast, one observes mainly periodic wrinkling (Auguste et al., 2017; Cai et al., 2011; 2012). Upon further compression or decrease of the contrast ratio, wrinkles transform into more complex morphologies, e.g., folds, creases, ridges (Auguste et al., 2017; Pocivavsek et al., 2008; Stoop et al., 2015; Wang and Zhao, 2013). In turn, the amplitude and wavelength of the patterns are a function of the thickness of the film as well as of the constitutive response of both the film and the substrate.

In the present work, the interest lies in the investigation of wrinkling-type instabilities present in magnetoelastic film-substrate systems subjected to combined magnetic and mechanical loads. Under purely magnetic loading,

* Corresponding author.
E-mail addresses: laurence.bodelot@polytechnique.edu (L. Bodelot), konstantinos.danas@polytechnique.edu (K. Danas).

https://doi.org/10.1016/j.jmps.2019.103734
0022-5096/

Moon and Pao (1969) studied the magnetoelastic buckling of a thin plate and Kankanala (2007) that of a rectangular beam, both subjected to a transverse magnetic field. When the magnetic field reaches a critical value, the plate and beam rotate, and the corresponding buckling wavelength is comparable to the finite length of the structure. This instability may be attributed to the well-known compass effect, i.e., the rotation and alignment of slender magnetic objects along the applied magnetic field in order to minimize their magnetic energy (or demagnetization energy). In this regard, when a thin magnetoelastic layer is now bonded to a non-magnetic soft substrate, the latter penalizes the energy of the long wavelength modes of the single magnetic layer, leading to finite wavelengths—hence wrinkling-type patterns—for the critical instability mode, as demonstrated theoretically by Danas and Triantafyllidis (2014) and experimentally by Psarra et al. (2017). More recently, Kalina et al. (2017) and Schümann et al. (2017) have replaced carbonyl iron by magnetically-hard NdFeB particles (Keip and Sridhar, 2019; Mukherjee and Danas, 2019), thus obtaining the so called h-MREs. Such materials exhibit strong magnetic hysteresis and permanent magnetization, while remaining fairly soft. These properties makes them excellent candidates for instability-controlled applications. In this regard, Kim et al. (2018) and Zhao et al. (2019) have used 3D-printing to fabricate and study the constitutive and bifurcated response of thin layers of h-MREs.

Such concepts are promising to obtain complex surface patterning with active control using a single and simple device. Indeed, even though mechanically-induced instabilities in planar geometries find applications in stretchable electronics, controllable stiffness devices, sensors and actuators (Lacour et al., 2004), the purely mechanical actuation of wrinkling in film-substrate systems does not allow for efficient, fast and versatile control of the surface patterns (Bowden et al., 1998; Huck et al., 2000), as opposed to the proposed system.

In this work, we study experimentally and numerically the behavior of a thin magnetorheological elastomer (MRE) layer bonded to a thick soft non-magnetic (passive) substrate as a function of pre-compression and applied magnetic field. The MRE film is made of an elastomer comprising randomly and isotropically dispersed iron particles (Bodelot et al., 2018), which are magnetically soft thus exhibiting no magnetic hysteresis. As a result, upon removal of the magnetic field, the surface patterns vanish. Specifically, we focus on the post-bifurcation film morphologies and their evolution with increasing magnetic field in a quantitative and qualitative manner. We show that under high pre-compression and increasing magnetic field, the wrinkling pattern transitions to a more complex morphology, called crinkling. It is demonstrated that the appearance of this mode can be related to a sharp curvature localization and a significant shearing of the lateral facets of the film. Similar crinkling patterns, albeit at the nanoscale, have only been recently observed in graphene (Kothari et al., 2018; Li et al., 2018) and have been directly associated with flexoelectricity effects (Kothari et al., 2019). In turn, in the present study, the same crinkling patterns are shown to be a result of strong magnetoelastic interactions in the intermediary air domain. In particular, the proposed numerical simulations allow to obtain a better insight into the crinkling mode observed experimentally and explain the physics behind it.

Following this introduction, we first present the experimental setup and data analysis in Section 2. Next, in Section 3, we discuss in detail the theoretical and numerical framework that is necessary for the analysis of the present boundary value problem. Then, we proceed in Section 4 to the qualitative and whenever possible quantitative comparison between the numerical and experimental results. We conclude the study in Section 5.

2. Experiments

In this section, we discuss the experimental analysis of the film profiles used to study the post-bifurcation response of the MRE film-substrate system. For completeness, we recall next some of the important features of the experiments described in Psarra et al. (2017).

2.1. Materials and fabrication

The film-substrate structure considered in this study is a 40 mm $\times$ 40 mm $\times$ 40 mm cube composed of an isotropic MRE film of thickness $h_f = 0.8$ mm and shear modulus G_f resting on a non-magnetic substrate of thickness $h_s = 39.2$ mm and shear modulus G_s. Note that the materials exhibit a quasi-incompressible response. Specific values for the compressibility are discussed in later.

Both the layer and the substrate are made of two-part soft silicone elastomers from Smooth-On Inc., USA. For the purely polymeric substrate, the two parts of Ecoflex 00-10 material (polymer and hardener) are mixed in a 1:1 weight ratio and degassed. For the MRE film, 20% volume fraction of carbonyl iron particles (CIP SM from BASF with median diameter 3.5 µm) are first dispersed into the polymer part of Ecoflex 00-50 material. Hardener is then added with a 1:1 polymer to hardener weight ratio and the compound is further mixed before being degassed. The MRE mixture is poured in a 40 mm $\times$ 40 mm $\times$ 0.8 mm mold base and the excess quantity is scraped away with a blade to get a flat film surface. Four 39.2 mm-height walls are subsequently mounted onto the base and the substrate mixture is poured on top of the film, up to the top of the walls. The film and the substrate are finally cured simultaneously to prevent film delamination. More details about the fabrication technique can be found in Psarra et al. (2017).

Because the film material is stiffer than the substrate material and is reinforced with particles, a stiffness contrast of $G_s/G_f = 0.3$ is obtained with $G_s = 3$ kPa. The film relative susceptibility $\chi_f = (\mu_f - \mu_0)/\mu_f$ (with μ_f and μ_0 denoting the magnetic susceptibility of the film and air, respectively) is evaluated at 0.4. These properties are reported in Table 1 and further details regarding their determination can be found in Psarra et al. (2017) as well as in Section 4.1.

Table 1
Material parameters used in the present calculations.

	G (kPa)	G' (kPa)	χ (-)	$\mu_0 m^s$ (T)
MRE film	10	1000	0.4	0.5
Passive substrate	3	300	0.0	0.0

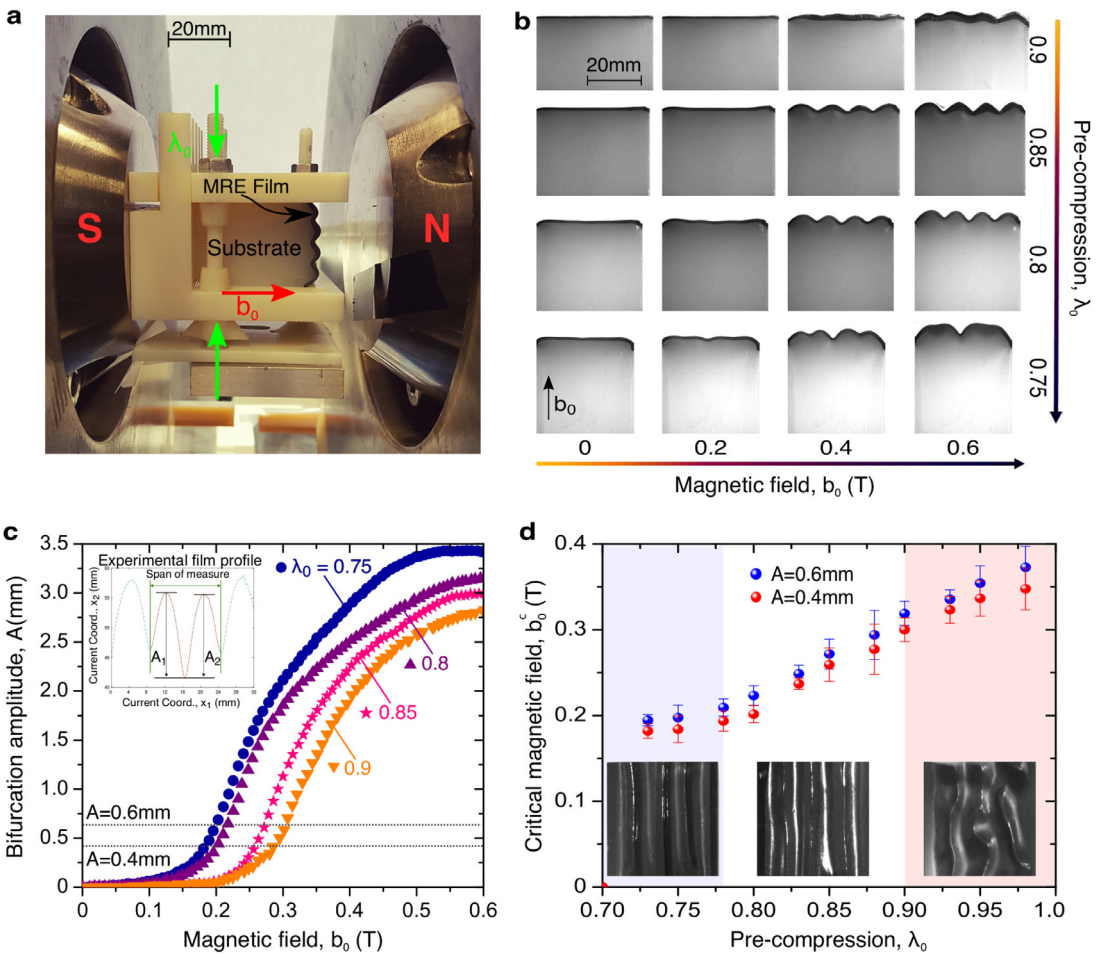

Fig. 1. (a) Custom-made setup for the magnetomechanical experiment. At first, the specimens are uniaxially compressed at a given stretch λ_0 with a non-magnetic screw-driven device. The pre-compression is fixed and the system is placed within the two poles of the electromagnet. The far magnetic field b_0 is then applied perpendicular to the film thickness in a linearly increasing fashion. A camera records the profile of the specimen that is subsequently used to analyze the bifurcation of the system. (b) Optical images of the morphological patterns versus the applied magnetic field b_0 for different pre-compressions λ_0. Scale bar, 20 mm. (c) Experimental measurements of the bifurcation amplitude A as a function of the magnetic field b_0, for different pre-compressions λ_0. A (in mm) denotes the average distance between peaks and valleys of the two central wrinkles (see inset). (d) Stability phase diagram of the corresponding morphological patterns in the two-field parameter space: mechanical pre-compression λ_0 and magnetic field b_0. The experimental (λ_0, b_0^c) critical points for 2D patterns (red), 1D patterns with descending b_0^c (white) and 1D patterns (blue) with saturated b_0^c are defined from the bifurcation curves in (c) by considering two thresholds $A = 0.4, 0.6$mm. Standard deviation of measurements from three specimens is included in the experimental data points. Parts of the exhibited curves and images are taken from Psarra et al. (2017). (For interpretation of the references to colour in this figure legend, the reader is referred to the web version of this article).

2.2. Magnetomechanical setup and experimental testing

To conduct the magneto-mechanical experiments, a compression device is 3D-printed using a non-magnetic polymeric material (Verowhite from Stratasys). It consists of three orthogonal walls forming a U shape. As can be seen in Fig. 1a, a non-magnetic screw-driven system allows to control the distance between the two parallel walls and thus to enforce different pre-compression stretch ratios λ_0. Before compression, silicone oil is applied onto the lateral faces of the film-substrate system in contact with the setup walls to decrease friction. However, the friction in these regions becomes significant at large pre-compressions and such boundary effects need to be taken into account in the numerical analysis (see Section 3).

The entire mechanically pre-compressed system is installed inside the 82 mm air gap separating the two 90 mm diameter poles of a two-coil electromagnet (see Fig. 1a), so that the magnetic field is perpendicular to the film thickness. Subsequently, as the magnetic field is increased from 0 to 0.6 T at a rate of 0.002 T/s, an external sensor measures the amplitude of the applied magnetic field and images of the film-substrate system are recorded using a digital camera system with a 12 μm-per-pixel resolution. The specimen is then magnetically and mechanically unloaded and may be tested again under another pre-compression value. It is perhaps relevant to note here that due to the relatively small mechanical rate-dependence of both the MRE film and the silicone substrate, as well as the negligible magnetic hysteresis in the MRE film (Bodelot et al., 2018), the order of application of the loads, i.e., mechanical and magnetic does not alter the observed critical fields and patterns. Nevertheless, applying first the magnetic field and then the mechanical one, would necessitate a substantially more complex experimental setup, that would still allow for a quantitative analysis of the bifurcation amplitudes.

Optical images taken during tests carried out at a different pre-compression λ_0 are reported in Fig. 1b. For all applied $\lambda_0 = 0.9, 0.85, 0.8$ and 0.75, the system eventually bifurcates as a result of the applied magnetic field b_0 and one can qualitatively observe a tendency of the critical magnetic field to decrease with increasing pre-compression (and vice versa). This magneto-mechanical morphological map also provides experimental evidence that different surface patterns can be formed with the film-substrate system by different combinations of pre-compressions and magnetic fields. For small pre-compressions (e.g., $\lambda_0 = 0.9$, first row of Fig. 1b), the wrinkling patterns are complex and two-dimensional (2D) as a consequence of the high in-plane symmetries of the cubic film-substrate system that retains an almost square top surface at small pre-compression. For higher pre-compression (e.g., $\lambda_0 = 0.85, 0.8$, second and third row of Fig. 1b), the in-plane square symmetry breaks, leading to a one-dimensional (1D) sinusoidal wrinkling-type pattern of single period and stable wavenumber ($\omega = 4$). Upon further pre-compression (e.g., $\lambda_0 = 0.75$, last row of Fig. 1b), the film-substrate system undergoes significant friction at its lateral faces in contact with the mechanical compression device, as evidenced by the presence of a non-negligible curvature at both sides of the film. Such a curvature tends to inhibit the full formation of mechanical wrinkling on the film, even though one reaches very close to the point of mechanical wrinkling, as discussed in more detail in Section 3.4. This promotes a period-doubling pattern at the post-bifurcation regime. Finally, note that at lower pre-compressions, increase of the magnetic field further intensifies the formed post-bifurcation pattern leading to the sharpening of the valleys. In a similar fashion, at high pre-compressions (i.e. $\lambda_0 < 0.8$), further increase of the magnetic field leads to other types of patterns (see last row of Fig. 1b) that evolve from period-doubling to a more localized sharp mode. These patterns, called "crinkles", are investigated in detail in the next Section.

To explore quantitatively the influence of the magneto-mechanical coupling over the critical loads and formed patterns, the film-substrate profiles obtained during the tests are analyzed by image processing. Grayscale images are binarized so that the background appears white and the film-substrate system appears black. The position of the film can then be identified as the interface between the white and black pixels, and the out-of-plane deflection of the film A can be computed as the average of the amplitudes (distance between a peak and a valley) measured on the two central wrinkles (both edge wrinkles are excluded from the analysis to avoid edge effects, see inset in Fig. 1c). In Fig. 1c, amplitude curves are plotted for all applied pre-compressions $\lambda_0 = 0.9, 0.85, 0.8$ and 0.75. The transition from the principal solution ($A = 0$) to the supercritical bifurcated branch is smooth and increases gradually with the magnetic field, indicating the presence of intrinsic geometrical and material imperfections deriving from the fabrication process. The bifurcation transition points (λ_0, b_0^c) are determined by setting a threshold over the amplitude ($A = 0.4$ or 0.6 mm) so that wrinkles are well-formed, whereas the threshold is in the same range with the film thickness h_f. This clearly shows in Fig. 1d, independently of the chosen threshold value, the decreasing trend of the critical magnetic field as a function of pre-compression. The evolution of the post-bifurcated morphology as a function of pre-compression is also highlighted in the insets at the bottom of the figure. Therein, we observe an evolution of 2D patterns at low pre-compression towards 1D cylindrical patterns at mild and high pre-compressions (from right to left). Note here that the setup described earlier does not allow the direct visualization and measurement of wrinkling from the top of the film. Here, a mirror making a 45° angle with the camera was used to take images from the surface of the film. Finally, we should note that more precise alternative methods, such as that of Diab et al. (2013) who use coefficients of the Fourier transform of the data, could be used to identify the wrinkling bifurcation. Nevertheless, the strong boundary effects in the present problem may lead to significant noise in such coefficients and thus the simpler threshold approach has been used in this case.

2.3. From wrinkling to crinkling and curvature localization

In this section, we study in detail the evolution of the post-bifurcation pattern upon further increase of the applied magnetic field. In Fig. 2, we consider the amplitude of two neighboring wrinkles. The amplitudes plotted in green correspond to the distance between the valley shown by the green arrow and the peak at its right, while the amplitudes plotted in red correspond to the distance between the valley shown by the red arrow and the common peak at its left. At low pre-compression ($\lambda_0 = 0.85$, see Fig. 2a), both amplitudes evolve similarly as the magnetic field increases (insets 1 and 2). At higher pre-compressions ($\lambda_0 = 0.78, 0.75$, Fig. 2b and c, respectively), the two amplitude curves diverge at a rather low critical magnetic field threshold (indicated by a dotted line) that decreases with increasing pre-compression, thus highlighting a secondary bifurcation that leads to a pattern morphology evolution. In particular, for $\lambda_0 = 0.78$ (Fig. 2b), the wrinkling pattern switches from sinusoidal (inset 1) to mild period-doubling (inset 2). For the $\lambda_0 = 0.75$ pre-compression (Fig. 2c), the secondary bifurcation arises very early and the pattern readily corresponds to a low-amplitude period doubling (inset

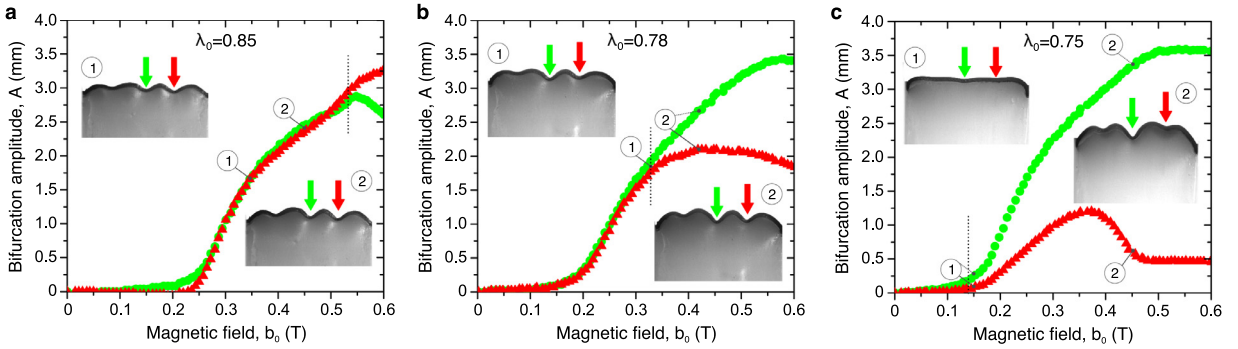

Fig. 2. Measurement of the bifurcation amplitude A versus the magnetic field b_0 of the central (green) and the right (red) wrinkle, for pre-stretch values (a) $\lambda_0 = 0.85$, (b) $\lambda_0 = 0.78$ and (c) $\lambda_0 = 0.75$. At high pre-compressions (b,c) a secondary bifurcation develops, leading to the splitting of the amplitude of two neighboring wrinkles. This splitting only occurs at very high magnetic field at lower pre-compressions (a). (For interpretation of the references to colour in this figure legend, the reader is referred to the web version of this article).

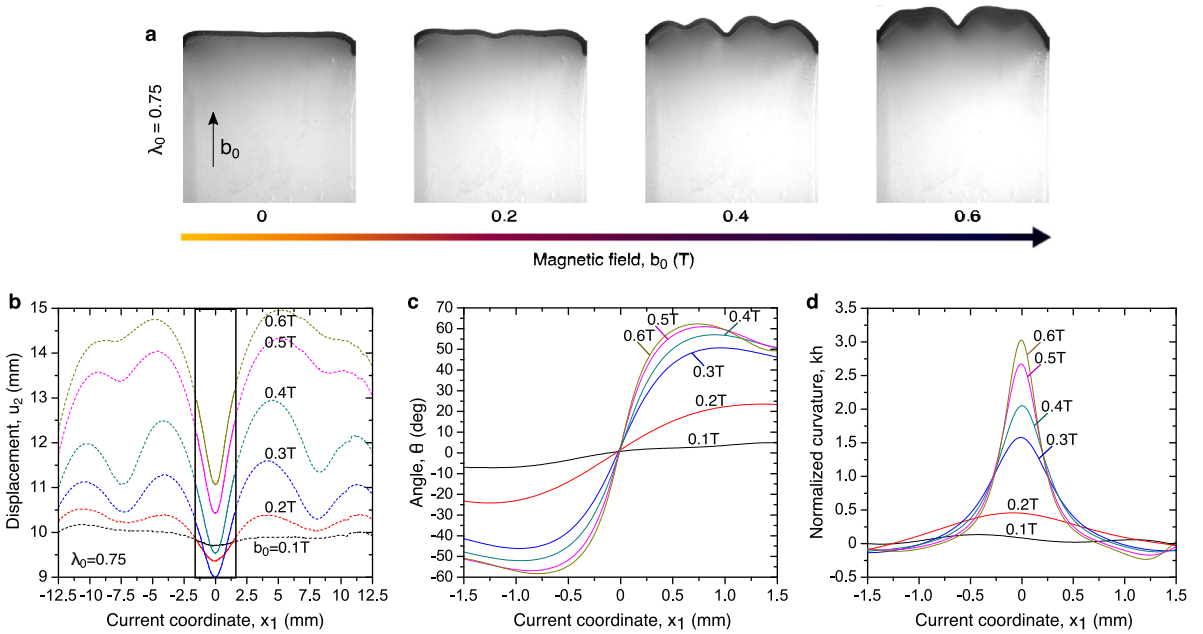

Fig. 3. Experimental results. (a) Morphological patterns with increasing magnetic field b_0 at $\lambda_0 = 0.75$. (b) Profile evolution of the displacement u_2 of the top surface of the MRE film at various applied magnetic fields b_0 as a function of the current coordinate x_1. (c) Evolution of the shear angle $\theta = \tan^{-1}(\partial u_2/\partial x_1)$ measuring the shearing of the faces of the central wrinkle-crinkle as a function of the current coordinate x_1. (d) Normalized curvature kh (with $h = h_f$ the film thickness) of the central wrinkle-crinkle as a function of the current coordinate x_1. Upon increase of the magnetic field b_0, the post-bifurcation mode evolves from quasi-smooth wrinkles to period-doubling and to a localized crinkle and curvature localization at the central part of the specimen.

1). It then further evolves into a more localized mode (inset 2) as the central wrinkle becomes deeper and sharper, though without self-contact of the free surface, while the side undulations see their amplitude decrease. In this case, following Kothari et al. (2018), we identify this mode as a "crinkle", a term introduced to describe a particular curvature localization mode producing shallow-kink corrugation in multi-layer graphene. As we will see in the following, this mode is also present at lower pre-compressions and at higher magnetic fields albeit exhibiting overall smaller amplitudes (Fig. 2a, inset 2).

The pattern morphology evolution at high pre-compression ($\lambda_0 = 0.75$) is further investigated in Fig. 3. Fig. 3a shows the different patterns obtained as the magnetic field increases and successive bifurcations occur. For different magnetic fields, different quantities related to the film are then plotted as a function of the current coordinate x_1. The displacement profile u_2 of the top surface of the MRE film is reported in Fig. 3b and is the quantitative counterpart of Fig. 3a. Now focusing the analysis at the center of the sample ($[-1.5; 1.5]$ mm range), the shear angle θ $(= \tan^{-1}(\partial u_2/\partial x_1))$ and the normalized curvature kh (with $h = h_f$ the film thickness) are reported in Fig. 3c and d, respectively. As the magnetic field increases, one notices a strong increase in the slope of the shear angle that leads to a sharp curvature localization at the central part of the film. The evolution into a crinkle pattern is thus accompanied by a strong curvature localization at the center of the

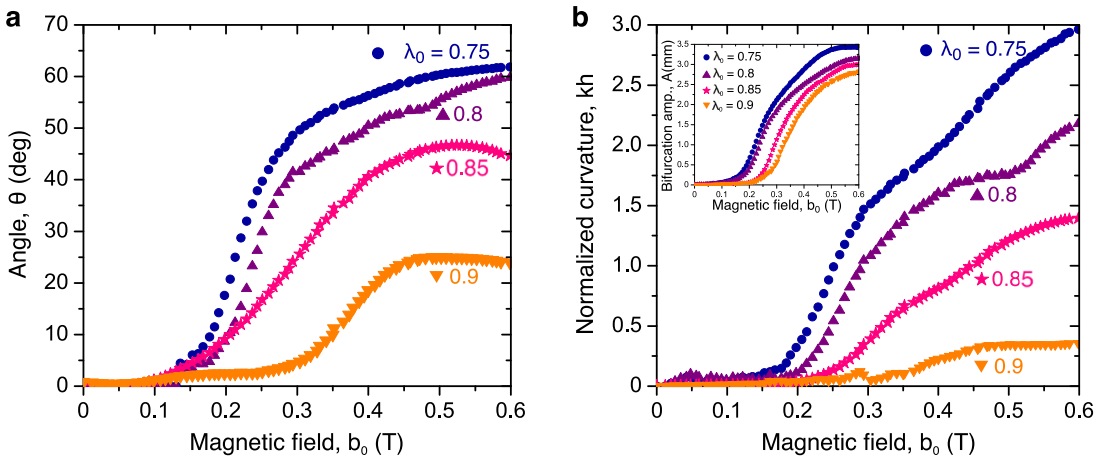

Fig. 4. Experimental evolution of (a) the shear angle θ and (b) the normalized curvature kh as a function of the applied magnetic field b_0 for various pre-compressions, $\lambda_0 = 0.75, 0.8, 0.85, 0.9$. Curvature localization appears in all pre-compressions considered here, $0.75 \leq \lambda_0 \leq 0.9$, albeit with decreasing amplitude for lower pre-compressions. All curves asymptote as a result of magnetic saturation.

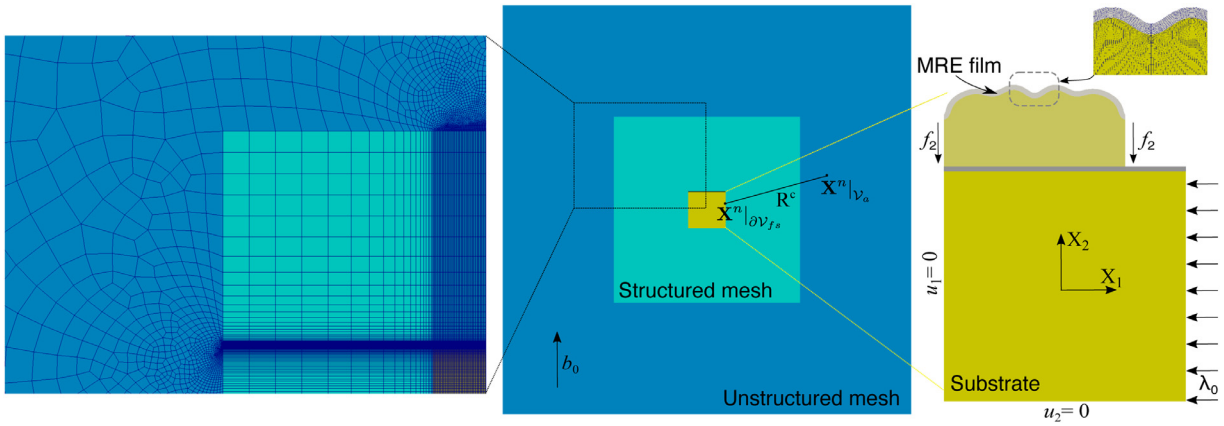

Fig. 5. Mesh of the air-film-substrate system. All regions are meshed with quadrilateral bilinear, 4-node isoparametric, (magneto-)mechanical elements. A structured mesh with deformable elements (light blue) is defined by the distance R_f from the solid boundary. The rest of the air region, defined by distance Δl_{air} from the solid boundary, is unstructured and stationary (dark blue). (For interpretation of the references to colour in this figure legend, the reader is referred to the web version of this article).

sample. As we explain in Section 4, the two opposite faces of the mid crinkle of the film never come into contact as long as the magnetic field is switched on, due to repelling magnetic forces. As a consequence, this phenomenon prohibits the formation of a crease or a fold in that region.

Finally, in Fig. 4, we examine the middle wrinkles for all pre-compressions considered in our experimental study, and analyze the shearing angle θ and normalized curvature localization kh. As one observes, crinkle patterns accompanied by significant shearing of the side faces of the film develop for all pre-compressions considered. The amplitudes of both θ and kh increase with the pre-compression similar to the bifurcation amplitude (see inset in Fig. 4b). This implies that crinkling is an intrinsic deformation mechanism in soft MREs and its physical interpretation is given in Section 4, where a full field numerical analysis allows to obtain the local magnetic and mechanical fields. Also, we observe in Fig. 4b that the curvature localization curves increase from a zero value at magnetic fields that are higher than those obtained for the corresponding wrinkling bifurcation in Fig. 1c. This directly suggests that this departure point from zero in Fig. 4b may be used as a potential criterion to identify the onset of the secondary crinkle bifurcation.

3. Variational formulation and numerical analysis

In this section, we present the variational formulation, geometry and choice of energies used to analyze the previously-described MRE film-substrate boundary value problem (BVP). The discussion that follows is based on the geometry and mesh of Fig. 5. Before we proceed to the specific discussion of the BVP at hand, we present briefly some preliminary definitions in the theory of magnetoelasticity.

3.1. Variational formulation

Without loss of generality, let us consider a magnetoelastic deformable solid that occupies a region $\mathcal{V}_0$ with external boundary $\partial\mathcal{V}_0$ of outward normal $\mathbf{N}$ in the undeformed stress-free configuration. Material points in the solid are identified by their initial position vector $\mathbf{X}$ in the undeformed configuration $\mathcal{V}_0$, while the current position vector of the same point in the deformed configuration is given by $\mathbf{x} = \boldsymbol{\chi}(\mathbf{X})$. Motivated by the usual physical arguments, the mapping $\boldsymbol{\chi}$ is required to be continuous and one-to-one on $\mathcal{V}_0$. In addition, we assume that $\boldsymbol{\chi}$ is twice continuously differentiable, except possibly on existing interfaces (e.g., due to the presence of different phases) inside the material. The deformation gradient is then denoted by $\mathbf{F} = \text{Grad}\,\boldsymbol{\chi}$ and its determinant by $J = \det\mathbf{F} > 0$. Here, Grad denotes the gradient operator with respect to $\mathbf{X}$ in the reference configuration. In addition, the reference density of the solid ρ_0 is related to the current density ρ by $\rho_0 = \rho J$. Time dependence or dissipation is not considered here.

In pure magnetics, the current magnetic field $\mathbf{b}$ is divergence-free, the $h-$field $\mathbf{h}$ is curl-free and the magnetization $\mathbf{m}$ per unit current volume is defined by

$$\mathbf{b} = \mu_0(\mathbf{h} + \mathbf{m}) \qquad \text{in} \quad \mathcal{V}, \tag{3.1}$$

where μ_0 is the magnetic permeability in vacuum (to be specified later) and $\mathcal{V}$ is the volume in the current configuration. This equation is used to identify one out of the three vector fields when one vector field is used as an independent variable and the other one is given by a constitutive equation, e.g., $\mathbf{h} = f(\mathbf{b})$. In general, and in purely mathematical terms, one could choose any of the above as an independent variable. Note, however, that $\mathbf{b}$ and $\mathbf{h}$ are *a priori* Eulerian quantities that need to satisfy differential constraints and boundary conditions, whereas the magnetization $\mathbf{m}$, which is also a Eulerian quantity by definition through Eq. (3.1), does not need to satisfy any differential constraints or interface conditions and thus makes it an intermediary variable that is not enough on its own to describe the entire BVP. At large strains, the fields $\mathbf{b}$ and $\mathbf{h}$ can be pulled back from $\mathcal{V}$ to $\mathcal{V}_0$ to their Lagrangian forms, denoted by $\mathbf{B}$ and $\mathbf{H}$, respectively, such that (Bustamante et al., 2008; Dorfmann and Ogden, 2003)

$$\mathbf{B} = J\mathbf{F}^{-1}\mathbf{b}, \qquad \mathbf{H} = \mathbf{F}^T\mathbf{h}. \tag{3.2}$$

No attempt is done to provide any Lagrangian form for $\mathbf{m}$ since that would be non unique and is of no use in the subsequent analysis. Moreover, as has been extensively discussed in the literature (see for instance Dorfmann and Ogden (2005)), Eq. (3.1) is not form invariant under transformations, which is a manifestation of the non-unique definition of $\mathbf{m}$. In the results sections, we report data for the current magnetization $\mathbf{m}$ as defined by the Eq. (3.1).

Motivated by the experimental observations at hand and recent experimental works by Danas et al. (2012) and Bodelot et al. (2018), the MRE materials are described in the present work by a free energy density $W(\mathbf{X}, \mathbf{F}, \mathbf{B})$. This energy can be split into a mechanical free energy density that is a function of the deformation gradient, $\mathbf{F}(\mathbf{X})$ and an magnetoelastic free energy that depends on $\mathbf{F}(\mathbf{X})$ and the magnetic field $\mathbf{B}(\mathbf{X})$ (Danas, 2017; Lefèvre et al., 2017; Ponte Castañeda and Galipeau, 2011). Specific definitions of these energies are provided in Section 3.3. Henceforth, the $\mathbf{X}$ argument will be dropped for simplicity of notation whenever considered unnecessary.

Following the work of Dorfmann and Ogden (2003), we define the potential energy of the system as

$$\mathcal{P}_0(\mathbf{u}, \mathbf{A}) = \min_{\mathbf{u}\in\mathcal{K}(\mathbf{F})}\min_{\mathbf{A}\in\mathcal{A}(\mathbf{B})}\int_{\mathcal{V}_0} W(\mathbf{F}(\mathbf{u}), \mathbf{B}(\mathbf{A}))\mathrm{d}V - \int_{\partial\mathcal{V}_0^T}\mathbf{T}_0\cdot\mathbf{u}\,\mathrm{d}S - \int_{\partial\mathcal{V}_0^\varphi}(\mathbf{H}_0\times\mathbf{A})\cdot\mathbf{N}\,\mathrm{d}S, \tag{3.3}$$

where $\mathcal{K}$ and $\mathcal{A}$ are the admissibility sets for the displacement field $\mathbf{u}$ and the magnetic vector potential $\mathbf{A}$ denoted by

$$\mathcal{K}(\mathbf{F}) = \{\mathbf{F} : \exists\mathbf{x} = \boldsymbol{\chi}(\mathbf{X}) \text{ with } \mathbf{F} = \mathbf{I} + \text{Grad}\mathbf{u},\ J > 0,\ \forall\mathbf{X}\in\mathcal{V}_0,\ \mathbf{u}(\mathbf{X}) = \mathbf{u}_0(\mathbf{X}) \text{ in } \partial\mathcal{V}_0^u\}, \tag{3.4}$$

and

$$\mathcal{A}(\mathbf{B}) = \left\{\mathbf{B} : \exists\mathbf{x} = \boldsymbol{\chi}(\mathbf{X}) \text{ with } \mathbf{B} = \text{Curl}\mathbf{A},\ \forall\mathbf{X}\in\mathcal{V}_0,\ \mathbf{A}(\mathbf{X})\times\mathbf{N} = \mathbf{A}_0(\mathbf{X})\times\mathbf{N} \text{ in } \partial\mathcal{V}_0^A\right\}, \tag{3.5}$$

respectively. In these last expressions, $\partial\mathcal{V}_0^u$, $\partial\mathcal{V}_0^T$, $\partial\mathcal{V}_0^A$ and $\partial\mathcal{V}_0^\varphi$ denote the portions of the boundaries where displacements $\mathbf{u}_0$, tractions T_0, vector potential $\mathbf{A}_0$ and scalar potential φ_0 ($\mathbf{H}_0 = -\text{Grad}\varphi_0$) are applied, respectively, while $\mathbf{N}$ denotes the unit normal to the corresponding boundary. Moreover, the introduction of $\mathbf{A}$ ensures that $\mathbf{B}$ is divergence free. By extremizing the potential energy $\mathcal{P}_0$ in (3.3) with respect to $\mathbf{u}$ and $\mathbf{A}$, one obtains the Euler-Lagrange field equations and the corresponding jump conditions at internal interfaces, S_i,

$$(\mathcal{P}_0)_{,\mathbf{u}}\delta\mathbf{u} = 0 \ \Rightarrow\ \text{Div}\mathbf{S} = \mathbf{0}, \quad \mathbf{S} = \frac{\partial W}{\partial\mathbf{F}}, \quad \forall\mathbf{X}\in\mathcal{V}_0, \qquad [\![\mathbf{S}]\!]\mathbf{N}_i = \mathbf{0}, \quad [\![\mathbf{N}]\!] = 0, \quad \forall\mathbf{X}\in S_i, \tag{3.6}$$

$$(\mathcal{P}_0)_{,\mathbf{A}}\delta\mathbf{A} = 0 \ \Rightarrow\ \text{Curl}\mathbf{H} = \mathbf{0}, \quad \mathbf{H} = \frac{\partial W}{\partial\mathbf{B}}, \quad \forall\mathbf{X}\in\mathcal{V}_0, \quad \mathbf{N}_i\times[\![\mathbf{H}]\!] = \mathbf{0}, \quad \forall\mathbf{X}\in S_i, \tag{3.7}$$

as well as the boundary conditions

$$\begin{aligned}&\mathbf{u} = \mathbf{u}_0, \quad \forall\mathbf{X}\in\partial\mathcal{V}_0^u, \qquad [\![\mathbf{S}]\!]\cdot\mathbf{N} = \mathbf{T}_0, \quad \forall\mathbf{X}\in\partial\mathcal{V}_0^T,\\ &\mathbf{A}\times\mathbf{N} = \mathbf{A}_0\times\mathbf{N}, \quad \forall\mathbf{X}\in\partial\mathcal{V}_0^A, \qquad \mathbf{N}\times\mathbf{H} = \mathbf{N}\times\mathbf{H}_0, \quad \forall\mathbf{X}\in\partial\mathcal{V}_0^\varphi.\end{aligned} \tag{3.8}$$

Here, $\mathbf{S}$ is the total first Piola-Kirchhoff stress, which comprises both the mechanical and the Maxwell stress contributions. These definitions are general and will be used in the following to define the response of each part of the BVP at hand.

3.2. BVP geometry, mesh and potential energies for each domain

In this section, we specify the potential energies for each domain of the BVP shown in Fig. 5. Specifically, we partition our BVP in three major domains: (i) the film occupying a volume $\mathcal{V}_f$, (ii) the substrate occupying a volume $\mathcal{V}_s$ and (iii) the air domain occupying a volume $\mathcal{V}_a$. This implies that the total potential energy of the problem is simply $\mathcal{P} = \mathcal{P}_f + \mathcal{P}_s + \mathcal{P}_a$. Each one of these potential energies is discussed in detail in the following two sections.

In turn, the air-film-substrate geometry is discretized and numerically simulated using the finite element (FE) method via the development of a user element in FEAP (Taylor, 2011). Furthermore, by assuming plane-strain conditions, which are consistent with the BVP of interest here—provided that a sufficient pre-compression is applied—one can study the bifurcation problem in two dimensions (2D). This is advantageous in the present context since it allows to deal more efficiently with larger local strains without need for re-meshing. For the numerical calculations, we use standard quadrilateral bilinear isoparametric elements that induce full continuity of the associated displacement and vector potential fields. Note that due to the 2D character of the analyzed problem, the vector potential is continuous everywhere and has only a non-zero out-of-plane component, i.e., $\mathbf{A} = \alpha\,\mathbf{e}_3$ as discussed in detail in the following.

3.2.1. Film and substrate geometry and potential energies

Specifically, the MRE film-substrate specimen has the same geometrical dimensions with that used in the experiments, i.e., $h_f = 0.8\,\text{mm}$ and $h_s = 39.2\,\text{mm}$, whereas both have a width $w_s = w_f = 40\,\text{mm}$. The out-of-plane dimension is inconsequential due to the imposed plane-strain conditions (and is taken to be 1 mm). Thus $\mathcal{V}_f \equiv [-h_f/2, h_f/2] \otimes [-w_f/2, w_f/2] \otimes [0,1]$ and $\mathcal{V}_s \equiv [-h_s/2, h_s/2] \otimes [-w_s/2, w_s/2] \otimes [0,1]$. The loading procedure is done in two steps similar to the experimental setup. First, we apply incrementally a pre-compression λ_0 along direction 1, i.e. $u_1 = \lambda_0 - 1$. For reasons that are discussed in detail in Section 3.4, we also apply transverse concentrated (shear) nodal forces along direction X_2, denoted by f_2, at the lateral faces of the film-substrate system. This is done to simulate approximately the friction due to the pre-compression device (see right sketch in Fig. 5). The bottom part of the substrate is fixed in the 2-direction, while the top part of the film is traction free. The interface between the film and the substrate is taken to be perfect with full displacement and traction continuity. The same is considered also for all interfaces (e.g., film-substrate, air-film and air-substrate) in the present BVP.

In this regard, we define the potential energies for the film, $\mathcal{P}_f$, and the substrate, $\mathcal{P}_s$, in the most general form. Following the definition (3.3), one can write compactly the two distinct potential energies as

$$\mathcal{P}_{(f,s)}(\mathbf{u},\alpha) = \min_{\mathbf{u}\in\mathcal{K}_{(f,s)}(\mathbf{F})} \min_{\mathbf{A}\in\mathcal{A}_{(f,s)}(\mathbf{B})} \int_{\mathcal{V}_{(f,s)}} W_{(f,s)}(\mathbf{F},\mathbf{B})\mathrm{d}V - \sum_{i=1}^{N_{\partial\mathcal{V}_{fs}}} f_2^{(i)} u_2^{(i)}, \tag{3.9}$$

where we denote compactly $\partial\mathcal{V}_{fs} \equiv (\partial\mathcal{V}_f \cup \partial\mathcal{V}_s) \cap \partial V_c$, with $\partial V_c \equiv \{(X_1,X_2) = (-w_s/2, -h_s/2),\ (X_1,X_2) = (w_s/2, h_s/2)\}$ such that $N_{\partial\mathcal{V}_{fs}}$ denotes all the nodes lying on the film-substrate boundary except the bottom left and right corner nodes of the substrate, where we apply displacement boundary conditions (see schematics in Fig. 5). In turn, $\mathcal{K}_f$, $\mathcal{K}_s$ and $\mathcal{A}_{(f,s)}$ become

$$\begin{aligned}\mathcal{K}_f(\mathbf{F}) = \{&\mathbf{F} : \exists \mathbf{x} = \boldsymbol{\chi}(\mathbf{X}) \text{ with } \mathbf{F} = \mathbf{I} + \mathrm{Grad}\mathbf{u},\ J > 0,\ \forall \mathbf{X} \in \mathcal{V}_f,\\ &u_1(-w_f/2, X_2) = 0, \quad u_1(w_f/2, X_2) = \lambda_0 - 1,\ \forall X_2 \in [-h_f/2, h_f/2]\},\end{aligned} \tag{3.10}$$

$$\begin{aligned}\mathcal{K}_s(\mathbf{F}) = \{&\mathbf{F} : \exists \mathbf{x} = \boldsymbol{\chi}(\mathbf{X}) \text{ with } \mathbf{F} = \mathbf{I} + \mathrm{Grad}\mathbf{u},\ J > 0,\ \forall \mathbf{X} \in \mathcal{V}_s,\\ &u_1(-w_s/2, X_2) = 0, \quad u_1(w_s/2, X_2) = \lambda_0 - 1,\ \forall X_2 \in [-h_s/2, h_s/2],\\ &u_2(X_1, -h_s/2) = 0, \forall X_1 \in [-w_s/2, w_s/2]\}\end{aligned} \tag{3.11}$$

and

$$\mathcal{A}_{(f,s)}(\mathbf{B}) = \{\mathbf{B} : \exists \mathbf{x} = \boldsymbol{\chi}(\mathbf{X}) \text{ with } \mathbf{B} = \mathrm{Curl}\mathbf{A},\ \mathbf{A}(X_1,X_2) = \alpha(X_1,X_2)\mathbf{e}_3,\ \forall \mathbf{X} \in \mathcal{V}_{(f,s)}\}. \tag{3.12}$$

3.2.2. Air geometry and potential energy

The air domain is decomposed in two subdomains, as shown in color in Fig. 5. The inner domain is meshed using a structured biased mesh allowing to resolve more efficiently the deformation near the boundary of the solid. For the outer domain, we use an unstructured mesh, which allows to reduce the total number of degrees of freedom in the problem since the magnetic fields are fairly uniform far from the film-substrate block.

The elements within the air domain are forced to deform via a constraint function that is discussed in the following to avoid severe mesh distortion near the film-substrate-air interfaces. This fictitious air deformation does not alter the solution of the BVP problem since the air mechanical energy is set equal to zero (i.e. zero Young's modulus). There exist different approaches to deal with a deformable air domain, but such a discussion is beyond the scope of the present study. In this work, we introduce a very efficient and simple way to deal with the deformability of the air by use of a constraint function that is described in the following steps.

(i) For all nodes lying in the air domain, $\mathcal{V}_a$, we find the closest node on the film-substrate specimen boundary, $\partial\mathcal{V}_{fs}$, by a simple search algorithm, thus defining a set of node pairs of size N_a (with N_a being the number of nodes in the air domain).

(ii) For each pair of air-solid nodes, we define first a distance coefficient

$$d_i^n = 1 - \frac{\left| X_i^n\big|_{\partial\mathcal{V}_{fs}} - X_i^n\big|_{\mathcal{V}_a} \right|}{R^c}, \tag{3.13}$$

such that the constraint function becomes

$$c_i^n = \begin{cases} d_i^n\, u_i^n\big|_{\partial\mathcal{V}_{fs}} - u_i^n\big|_{\mathcal{V}_a} = 0, & \text{if} \quad 0 < d_i^n \leq 1 \\ u_i^n\big|_{\mathcal{V}_a} = 0, & \text{otherwise.} \end{cases} \tag{3.14}$$

Here, $n \in [1, N_a]$ denotes the pair number, $i = 1, 2$ the displacement degree of freedom and R^c the distance at which the constraint is applied along each direction i. Beyond that distance R^c per direction the corresponding displacement degrees of freedom for the air nodes are set equal to zero. In this example, the structured air subdomain is spatially defined by a square of side length $2R^c + w_f$ with R^c, concentric to the film-substrate domain. We set $R^c = 0.5(w_a - w_f)/2$, where $w_a = h_a$ denote the side lengths of the entire air domain (see Fig. 5). The coefficient of the first term in the constraint function in (3.14) ensures a linearly regressing displacement field in the air domain with increasing distance from the specimen boundary such that $u_i^n\big|_{\mathcal{V}_a} = 0$ at $\left| X_i^n\big|_{\mathcal{V}_a} \right| = \left| X_i^n\big|_{\partial\mathcal{V}_{fs}} \right| + R^c$.

(iii) The above constraint function can be enforced either by use of a Lagrange multiplier or a penalty formulation. For simplicity, we choose the second option and we define the penalty energy of the deformable air

$$\rho_0 \Phi_{pen}(\mathbf{u}) = \sum_{n=1}^{N_a} \sum_{i=1}^{2} \frac{G_c}{2\xi L_c^2} (c_i^n)^2, \tag{3.15}$$

where c_i^n is defined in (3.14), $L_c = 1\,\text{mm}$ is an arbitrary reference length and G_c is an arbitrary shear modulus that can be set equal to that of the film or the substrate. The latter is added to make ξ dimensionless. This term has to be added to the potential energy of the air domain.

One needs then to choose a fairly small value for ξ (to be defined later) such that the constraint function is satisfied to a sufficient accuracy. A larger value for ξ is also acceptable since the deformation of the air subdomain is inconsequential to the total potential energy of the system. The choice of ξ is mainly decided by numerical convergence studies and in the present study is set equal to $\xi = 10^{-7}$. Specifically, the proposed penalty approach leads in this case of wrinkling to accurate results and significantly better convergence than that of using small but finite shear and bulk moduli for the air domain. The above penalty function can be easily applied in any commercial code by defining "contact-type" user elements between two degrees of freedom[1].

Following the previous definitions, we define next the potential energy of the deformable air subdomain by

$$\mathcal{P}_a(\mathbf{u}, \alpha) = \min_{\mathbf{u} \in \mathcal{K}_a(\mathbf{F})} \min_{\mathbf{A} \in \mathcal{A}_a(\mathbf{B})} \int_{\mathcal{V}_a} \rho_0 \Phi_{pen}(\mathbf{u}) \mathrm{d}V + \int_{\mathcal{V}_a} \frac{1}{2\mu_0 J} \mathbf{FB} \cdot \mathbf{FB}\, \mathrm{d}V, \tag{3.16}$$

where $\mathcal{K}_a$ and $\mathcal{A}_a$ become

$$\begin{aligned} \mathcal{K}_a(\mathbf{F}) = \{ & \mathbf{F} : \exists \mathbf{x} = \boldsymbol{\chi}(\mathbf{X}) \text{ with } \mathbf{F} = \mathbf{I} + \mathrm{Grad}\mathbf{u},\ J > 0,\ \forall \mathbf{X} \in \mathcal{V}_a, \\ & \mathbf{u} = \mathbf{0}, \quad \forall \left| X_i^n\big|_{\partial\mathcal{V}_{fs}} \right| + R^c < \left| X_i^n\big|_{\mathcal{V}_a} \right| \leq |w_a|, \quad i = 1, 2\}, \end{aligned} \tag{3.17}$$

and

$$\begin{aligned} \mathcal{A}_a(\mathbf{B}) = \{ & \mathbf{B} : \exists \mathbf{x} = \boldsymbol{\chi}(\mathbf{X}) \text{ with } \mathbf{B} = \mathrm{Curl}\mathbf{A},\ \mathbf{A}(X_1, X_2) = \alpha(X_1, X_2)\mathbf{e}_3,\ \forall \mathbf{X} \in \mathcal{V}_a \\ & \alpha(X_1, X_2) = \epsilon_{ij} (B_0)_i X_j = \epsilon_{ij} (b_0)_i X_j, \quad X_i \in \partial\mathcal{V}_a\}. \end{aligned} \tag{3.18}$$

In the above equation, the Lagrangian, $\mathbf{B}_0$, and Eulerian, $\mathbf{b}_0$, magnetic fields are equal since $\mathbf{F} = \mathbf{I}$ in the stationary air subdomain, whereas ϵ_{ij} denotes the alternating symbol in 2D.

3.3. Choice of energy functions

In this section, we propose simple but sufficiently rich energy density functions to describe the constitutive response of the film and substrate magnetoelastic materials. The interest in this study is the modeling of MRE materials which can be either magnetoelastic or purely elastic. In this regard, it is convenient to characterize their constitutive behaviors in a

[1] While our calculations have been mainly carried out using the FEAP (Taylor, 2011) finite element code, additional calculations have also been done using Abaqus (2018) leading to exactly the same results. In the later case, use of the "*EQUATION" command to impose the constraint function gave the same results. This command is used for linear constraints as is the case in Eq. (3.14) and uses a direct elimination of the air nodes used in the constraint function.

Lagrangian formulation by free energies $W(\mathbf{F},\mathbf{B})$. These functions are suitably amended in order to include the contribution of the Maxwell stress and read (Dorfmann and Ogden, 2005)

$$W(\mathbf{F},\mathbf{B}) = \rho_0\Phi(\mathbf{F},\mathbf{B}) + \frac{1}{2\mu_0 J}\mathbf{F}\mathbf{B}\cdot\mathbf{F}\mathbf{B}, \tag{3.19}$$

where $\Phi(\mathbf{F},\mathbf{B})$ is the specific free-energy density to be defined below. The second term in the above equation is considered so that the total first Piola-Kirchhoff stress, $\mathbf{S}$, and the Lagrangian h-field, $\mathbf{H}$, are simply given by

$$\mathbf{S} = \frac{\partial W}{\partial \mathbf{F}}(\mathbf{F},\mathbf{B}), \qquad \mathbf{H} = \frac{\partial W}{\partial \mathbf{B}}(\mathbf{F},\mathbf{B}). \tag{3.20}$$

A number of energy functions—isotropic and anisotropic—have been proposed in the literature. Those can be divided to the phenomenological ones (Bustamante, 2010; Danas et al., 2012) and to those based on rigorous analytical homogenization methods (Galipeau and Ponte Castañeda, 2013; Lefèvre et al., 2017). In the present context of a passive substrate and thin films, the wrinkling response is mainly driven by the geometry of the BVP and thus simpler energy density functions largely suffice to reveal and capture the observed patterns, discussed in the experiments Section 2. In the following, we choose the same energy functions for the film and the substrate, whereas specific values for the constitutive parameters are reported later in Table 1 in Section 4.1.

In this regard, for a homogeneous magnetoelastic solid, we consider the following energy density

$$\begin{aligned}\rho_0\Phi(\mathbf{F},\mathbf{B}) &= \rho_0\Phi_{mech}(\mathbf{F}) + \rho_0\Phi_{mag}(\mathbf{F},\mathbf{B})\\ &= \rho_0\phi_{mech}(\mathbf{F}) + \rho_0\phi_{mag}(\mathbf{F},\mathbf{b}) = \rho_0\phi(\mathbf{F},\mathbf{b}).\end{aligned} \tag{3.21}$$

Use has been made of relation $(3.2)_1$ to obtain the property $\Phi(\mathbf{F},\mathbf{B}) = \Phi(\mathbf{F}, J^{-1}\mathbf{F}^{-1}\mathbf{b}) = \phi(\mathbf{F},\mathbf{b})$, while the term with subscript "mech" in the above equation denotes the purely mechanical contribution. Following the earlier work of Psarra et al. (2017), we describe the mechanical response by a Neo-Hookean model, i.e.,

$$\rho_0\Phi_{mech}(\mathbf{F}) = \frac{G}{2}(\mathbf{F}\cdot\mathbf{F} - 3 - 2\ln J) + \frac{G'}{2}(J-1)^2, \tag{3.22}$$

where G is the shear modulus and G' is the Lamé constant associated with the compressible part. In turn, for the magnetomechanical part, we use a magnetization saturation Langevin model, which reads

$$\rho_0\Phi_{mag}(\mathbf{F},\mathbf{B}) = \frac{J\mu_0\,(m^s)^2}{3\chi}\left\{\ln\left[\frac{3\chi}{\mu_0 m^s J}\sqrt{\mathbf{FB}\cdot\mathbf{FB}}\right] - \ln\left[\sinh\left(\frac{3\chi}{\mu_0 m^s J}\sqrt{\mathbf{FB}\cdot\mathbf{FB}}\right)\right]\right\}, \tag{3.23}$$

or equivalently in terms of the Eulerian $\mathbf{b}$

$$\rho_0\phi_{mag}(\mathbf{F},\mathbf{b}) = \frac{J\mu_0\,(m^s)^2}{3\chi}\left\{\ln\left[\frac{3\chi}{\mu_0 m^s}|\mathbf{b}|\right] - \ln\left[\sinh\left(\frac{3\chi}{\mu_0 m^s}|\mathbf{b}|\right)\right]\right\}. \tag{3.24}$$

In these two expressions, $|\mathbf{b}| = \sqrt{\mathbf{b}\cdot\mathbf{b}}$, μ_0 is the magnetic permeability in vacuum (to be specified later), m^s is the magnetic saturation and χ is the magnetic susceptibility. There are more than one definitions of magnetic susceptibility in the literature. The one used here is the more recent one in the bibliography whereas the classical one is $\chi_v = \chi/(1-\chi)$. For instance, in the absence of mechanical fields (e.g., rigid solids), the relative permeability $\mu = (1+\chi_v)\mu_0 = \mu_0/(1-\chi)$ of iron could be in the order of $\chi_v \approx 10-200$ or $\chi \approx 0.9-0.995$.

The magnetization is then defined by simple derivation of Eq. (3.24) (the same result could be obtained by proper derivation of (3.23) but is much more tedious) as

$$\begin{aligned}\mathbf{m} &= -\frac{\rho_0}{J}\frac{\partial\phi}{\partial\mathbf{b}} = -\frac{\rho_0}{J}\frac{\partial\phi_{mag}}{\partial\mathbf{b}} = -\frac{\rho_0}{J}\frac{\partial\Phi_{mag}}{\partial\mathbf{B}}\mathbf{F}^{-T}\\ &= \left(\frac{m^s}{|\mathbf{b}|}\coth\left[\frac{3\chi\,|\mathbf{b}|}{\mu_0 m^s}\right] - \frac{\mu_0\,(m^s)^2}{3\chi\,|\mathbf{b}|^2}\right)\mathbf{b},\end{aligned} \tag{3.25}$$

so that $\mu_0\mathbf{h} = \mathbf{b} - \mu_0\,\mathbf{m}(\mathbf{b})$. The magnetization response corresponding to energy density (3.24) is shown in Fig. 6 as a function of the magnetic field $\mathbf{b}$. In the limit of small magnetic fields, $\mathbf{B}\to\mathbf{0}$, one can show that the energy (3.24) becomes quadratic in $\mathbf{B}$ or $\mathbf{b}$, respectively, such that

$$\rho_0\Phi_{mag}(\mathbf{F},\mathbf{B}) = -\frac{\chi}{2\mu_0 J}\mathbf{F}\mathbf{B}\cdot\mathbf{F}\mathbf{B} = -\frac{J\chi}{2\mu_0}\mathbf{b}\cdot\mathbf{b} = \rho_0\phi_{mag}(\mathbf{F},\mathbf{b}). \tag{3.26}$$

This last case corresponds to ideal magnetic materials with no saturation. Using Eq. (3.25), one can easily show that the magnetization in this last case is linear in $\mathbf{b}$ and is given by

$$\mu_0\mathbf{m} = \chi\mathbf{b} \qquad \text{or} \qquad \mu_0\mathbf{h} = (1-\chi)\,\mathbf{b}. \tag{3.27}$$

We close this subsection by noting that the present choice of energy functions is the simplest possible that allows for a satisfactory quantitative and very good qualitative agreement with the experimental data presented previously. Those energies lead to negligible magneto-mechanical coupling in terms of pure material magnetostriction (Danas, 2017) and thus

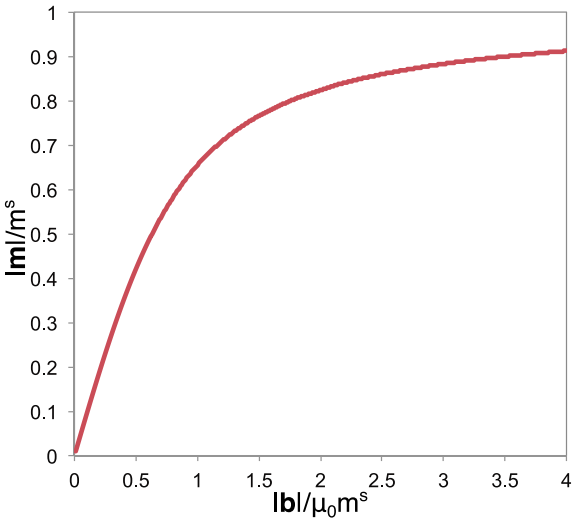

Fig. 6. A representative example of a $m-b$ response as obtained by the energy density described in Eq. (3.25) in the purely magnetic case, i.e., $\mathbf{F}=\mathbf{I}$ and $J=1$, and for a magnetic susceptibility $\chi=0.995$.

are expected to be less accurate deep in the post-bifurcation regime, especially when crinkles develop substantially due to the large shear strains obtained in that case. For a better agreement, one should resort to more elaborate magneto-mechanical models such as the one proposed recently by Lefèvre et al. (2017). Such a work is in progress and will be presented elsewhere.

3.4. Representative numerical results and effect of the transverse force f_2

In this section, we discuss the effect of the applied transverse force f_2 on the bifurcation response of the film-substrate system. As already discussed briefly in Psarra et al. (2017), we apply a transverse force f_2 (as sketched in Fig. 5) in order to mimic the frictional forces exerted by the lateral walls of the compressive device on the film-substrate specimen in the actual experiments (see Fig. 1a). Here, we carry out a more detailed quantitative study of this transverse force. The corresponding results are reported in Fig. 7.

In Fig. 1b, the experimental profiles clearly show a gradually developing curvature at the lateral boundaries of the film-substrate sample. This curvature becomes more significant with increase of the applied pre-compression. In this study, we do not attempt to measure exactly that curvature but instead we identify the applied transverse force f_2 by using the wrinkling amplitude curves. In this regard, we choose a very simple linear dependence of the transverse force on the applied axial pre-stretch λ_0, which reads

$$f_2 = f_c\,(\lambda_0 - 1), \quad f_c > 0, \quad 0 < \lambda_0 \leq 1. \tag{3.28}$$

In this expression, f_c is a positive constant that has the units of force and is denoted henceforth as transverse force coefficient. This constant will be calibrated by the wrinkling experiments as explained in detail in the following. But before, it is perhaps worth to comment further on Eq. (3.28). One can observe that due to the nonlinear neo-Hookean energy (3.22) used for the film and substrate mechanical response, the Piola-Kirchhoff component S_{11} is a nonlinear function of $\lambda_1=\lambda_0$ (and λ_2) and thus the transverse force f_2 depends nonlinearly on the normal reaction forces f_1 (which are directly related to S_{11}). Therefore, the approximate relation in (3.28) can be rationalized as an explicit approximation of a nonlinear friction-type law.

Specifically, in Fig. 7a, we show at the left column the corresponding experimental profiles for an applied pre-compression $\lambda_0=0.75$ and varying magnetic field $b_0=0, 0.2, 0.4\,\mathrm{T}$. A major observation in the context of the experiments is that the strong lateral friction induces a curvature of film near the lateral edges, which in turn delays (and even eliminates) the mechanical wrinkling. Subsequent application of the magnetic field triggers the magneto-mechanical wrinkling. This observation is in fact rationalized and validated by the corresponding FE simulations. Specifically, for $f_c=0$, a clear mechanical wrinkling mode is obtained for $\lambda_0\sim 0.76$ and no applied magnetic field. This is in quantitative agreement with numerous theoretical bifurcation studies in infinite film-substrate systems (see for instance Cao and Hutchinson, 2012; Danas and Triantafyllidis, 2014), which suggest a critical mechanical bifurcation stretch at $\lambda_0^{c,mech}=0.785$ for the choice of material parameters in the present study. Presently, we find a critical stretch $\lambda_0^{c,mech,FE}\sim 0.76$, which is a result of the finite slenderness of the film, $h_f/w_f=0.8/40=0.02$ and the Dirichlet boundary conditions considered.

Next, in Fig. 7a, by considering a non-zero transverse force coefficient $f_c=0.15, 0.3\,\mathrm{mN}$, we observe an induced curvature of the film near the lateral faces and almost complete annihilation of the purely mechanical wrinkling mode. Application

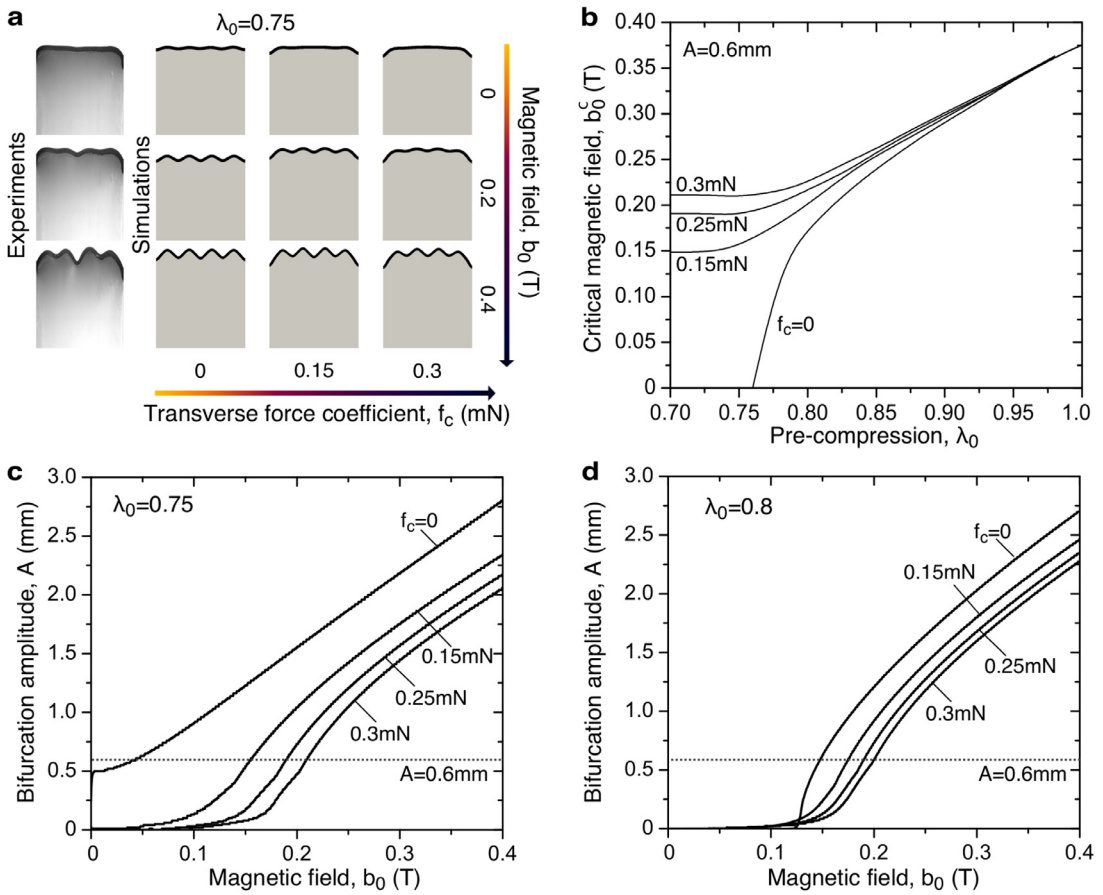

Fig. 7. (a) Qualitative comparison of experimental (left column) and numerical (right columns) profiles. The effect of friction as measured by the transverse force $f_2 = f_c\,(\lambda_0 - 1)$ on the lateral faces of the film-substrate block is shown for the numerical calculations. Increase of f_2 delays and even eliminates initial mechanical wrinkling. (b) Effect of friction on the numerical critical magnetic field, b_0^c, and applied pre-compression λ_0 map. Numerical bifurcation amplitude response for different transverse force coefficients f_c for (c) $\lambda_0 = 0.75$ and (b) $\lambda_0 = 0.8$ as a function of the applied magnetic field b_0. The dashed line indicates the threshold used to reconstruct the map in part (b).

of a magnetic field triggers subsequently the magneto-mechanical wrinkling modes, whereas for large f_c (or f_2), we can even observe an asymmetric increase of the wrinkle amplitudes at different positions in the film (e.g., see deformed shape corresponding to $f_c = 0.3$ mN and $b_0 = 0.4$ T). Such asymmetry is consistent with the experimental observations in Fig. 1b and Fig. 2 (see insets), although the FE calculations tend to underestimate it.

In order to quantify the above observations we show on Figs. 7c,d the evolution of the wrinkling amplitude, A, of the two central wrinkles, as already discussed in the inset of Fig. 1c for $\lambda_0 = 0.75$ and 0.8, respectively. The major observation in the context of Fig. 7c, corresponding to $\lambda_0 = 0.75$, is the transition from a mechanically wrinkled state at $b_0 = 0$ (see curves corresponding to $f_c = 0$) with a finite value of A to an unwrinkled mechanical state with $A = 0$ for finite $b_0 > 0$ and $f_c > 0$. In turn, for $\lambda_0 = 0.8$, the film-substrate system has not yet reached the mechanical wrinkled state and thus wrinkling occurs only by application of b_0. In this case, the application of the transverse force $f_c > 0$ delays the development of magneto-mechanical wrinkling. Finally, the combined bifurcation response for a wrinkling amplitude $A = 0.6$ mm is shown in Fig. 7b in the space of pre-compression λ_0 and applied critical magnetic field b_0^c. In this bifurcation phase diagram, we observe the seamless transition from a mechanically wrinkled state ($f_c = 0$) to an only magneto-mechanically wrinkled state for $f_c = 0.15, 0.25, 0.3$ mN. Increase of the transverse force f_c leads to increase of the critical magnetic field b_0^c. On the other hand, increase of the applied pre-compression λ_0 (at least) up to values of 0.7 does not alter the critical magnetic field b_0^c for a given $f_c > 0$ as revealed by the asymptotic response of b_0^c in that regime. In the subsequent comparisons with the experimental results, f_c serves as a fitting parameter and the value of $f_c = 0.25$ mN is found to deliver the best results.

It is important, however, to remark that the application of nodal forces leads to results that depend each time on the mesh, especially when the mesh is non-uniform. Specifically, by increasing the density of the mesh (see Fig. 5) closer to the film, we effectively induce a higher friction in that region for the same applied force f_2. This allows, in turn, for a fairly faithful representation of the curvature of the specimen at the lateral edges as shown in Figs. 7a. An alternative option, which would lead to mesh insensitive results, would be the application of a distributed load and thus an applied traction

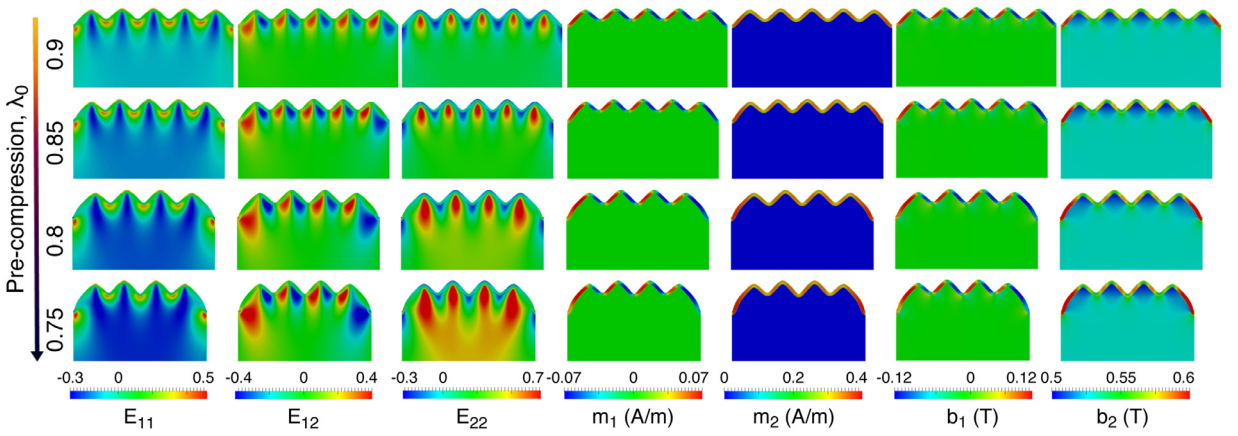

Fig. 8. Numerical contours of the Green-Lagrange strains, E_{11}, E_{12}, E_{22}, the magnetization components m_1, m_2 and the magnetic field b_1, b_2, obtained at $b_0 = 0.5\,\mathrm{T}$ and friction force coefficient $f_c = 0.25\,\mathrm{mN}$ for various pre-compressions λ_0.

on the lateral surfaces. By carrying out such a study, we have observed a less faithful representation of the curvature near the film-substrate lateral edges but not a significant effect on the obtained critical wrinkling magnetic fields. In any case, the presented results use the given mesh shown in Fig. 5 and the nodal transverse force friction law (3.28).

We close this section by showing in Fig. 8 numerical contours of an MRE film on a passive substrate for various pre-compressions $\lambda_0 = 0.75, 0.8, 0.85, 0.9$, $b_0 = 0.5\,\mathrm{T}$ and $f_c = 0.25\,\mathrm{mN}$. The contours depict different fields such as the Green-Lagrange strains, E_{11}, E_{22} and E_{12}, the magnetization components m_1 and m_2 and the current magnetic field components, b_1 and b_2. An important observation in the context of these results is that the numerical predictions of the pattern wavenumber is in very good agreement with the corresponding experimental ones for $\lambda_0 = 0.75, 0.8$, i.e., they predict four wrinkles. In turn, for $\lambda_0 = 0.85, 0.9$ the numerical simulations predict five undulations, which are closer in number to the theoretical results of Cao et al. (2014). This difference can be partially attributed to the fact that as pre-compression becomes smaller (i.e. $\lambda_0 \to 1$) two-dimensional surface patterns start occuring in the experiments (see inset in Fig. 1d). In this case, the two-dimensional plane-strain calculations carried out here, gradually lose their direct validity by comparison to the experiments. A second additional explanation can be given by performing a theoretical bifurcation analysis of an infinite film-substrate-air system such as the one described in Danas and Triantafyllidis (2014). In such an analysis, one can show that for the parameters used in the present calculations the critical wavenumber leads to patterns in between four and six wrinkles. In the present Dirichlet BVP the wavenumber of five wrinkles is picked by the FE calculation for $\lambda_0 \geq 0.85$ and that of four wrinkles for $\lambda_0 \leq 0.8$.

4. Numerical simulations versus experiments

In this section, we compare qualitatively and quantitatively the numerical and experimental results. Specifically, we first compare the effect of pre-compression λ_0 on the critical magnetic field b_0^c required for bifurcation at the early stages wrinkling. Subsequently, we analyze the shear angle and curvature localization of the central wrinkle into a crinkle and probe the corresponding experimental response. We then use the full-field simulations to provide a physics-based explanation on the formation of the crinkle pattern and show in more details the underlying mechanical and magnetic fields involved in this process.

4.1. Wrinkling amplitude

In this section, for completeness in the presentation of the results and the analysis, we recall and extend the main results obtained in Psarra et al. (2017). In that study, we have identified the material parameters of our film-substrate by use of different experiments. Specifically, the MRE film comprises iron particles at a 20vol%. Its magnetic permeability μ_f is measured with a Bartington MS2G sensor and is used to obtain the relative film susceptibility $\chi_f = 0.4$, reported in Table 1, from the relation $\chi_f = \left(\mu_f - \mu_0\right)/\mu_f$, with $\mu_0 = 4\pi\,10^{-7}\ \mathrm{NA}^{-2}$ the magnetic permeability of vacuum. In turn, the saturation magnetization of the MRE material is independent of the mechanical properties and the microstructure and is obtained by the simple rule of mixtures (Danas, 2017). By using earlier experimental results in similar materials (Danas et al., 2012), we use for the carbonyl iron a saturation magnetization $\mu_0 m^s_{iron} = 2.5\,\mathrm{T}$, which gives $\mu_0 m^s_f = 0.5\,\mathrm{T}$ for the MRE film (see Table 1) if mixed at $c = 20\%$ with a non-magnetic polymeric matrix. The shear modulus of the substrate G_s is obtained by an independent tensile experiment and is reported also in Table 1.

In order to obtain the shear modulus of the MRE film as well as the frictional transverse force coefficient f_c, we use two of the bifurcation amplitude curves obtained experimentally at pre-compression $\lambda_0 = 0.75$ and 0.85 (see Fig. 9a). The

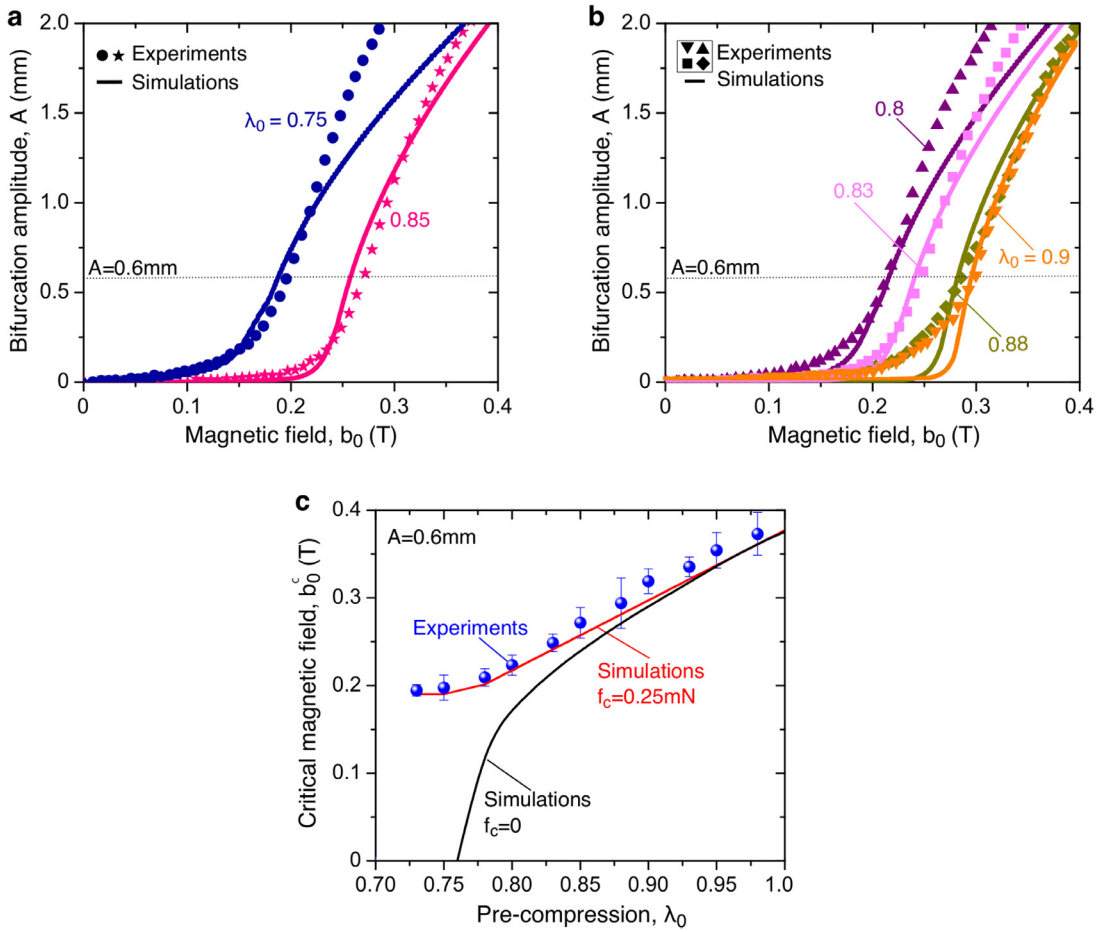

Fig. 9. Experiments vs. numerical simulations. (a-b) Bifurcation amplitude curves as a function of the applied magnetic field, b_0, for various pre-compressions, λ_0. (a) The two curves shown are used for the identification of the MRE shear modulus and friction force f_2. (b) Comparison between numerical predictions and experiments. (c) Two-field map, $\lambda_0 - b_0^c$, showing the numerical predictions with ($f_2 = 0.25$ mN) and without ($f_2 = 0$ mN) lateral friction forces.

transverse force coefficient is found to be $f_c = 0.25$ mN and $G_f = 10$ kPa as reported in Table 1. Given that both the MRE film and the substrate are fairly incompressible, we have considered Lamé constants associated with the compressibility that are ~ 100 times larger than the shear moduli of each phase (see Table 1). Given that the substrate has a modulus of $G_s = 3$ kPa, a mechanical substrate-to-film stiffness ratio $G_s/G_f = 0.3$ is obtained. In turn, the magnetic contrast between the film and the substrate is infinite in the present case. Note, however, that due to the nonlinear dependence of the energy density on the magnetic saturation m^s (see Eq. (3.25)), the bifurcation response cannot be related simply to mechanical and magneto-mechanical ratios in the present context.

The material parameters reported in Table 1 are shown in Fig. 9b to be sufficient to probe the rest of the experimental curves accurately enough for a large range of applied magnetic fields and pre-compressions. In Fig. 9c, we show the excellent quantitative agreement between the FE simulations and the experiments for the critical bifurcation loads in the case of a transverse force coefficient $f_c = 0.25$ mN. For comparison, we show also the curve corresponding to $f_c = 0$, which as expected reaches the $b_0 = 0$ axis at a pre-compression of $\lambda_0 \sim 0.76$. In this last frictionless case, a pre-compression beyond $\lambda < 0.76$ leads to mechanical wrinkling as discussed already in the context of Fig 7. This last observation reveals clearly the importance of including the frictional effects induced by the lateral walls of the pre-compression device.

4.2. Numerical curvature localization and crinkling mechanisms

The comparisons of the previous section provide sufficient confidence to use the numerical simulations as a means to understand the physical mechanisms that allow the smooth wrinkle patterns to evolve to crinkles, i.e., patterns with pronounced curvature localization.

We specialize the discussion next to the case of large pre-compressions, $\lambda_0 = 0.75$ and $f_c = 0.25$ mN. Specifically, Fig. 10a shows numerical snapshots at different applied magnetic fields $b_0 = 0, 0.2, 0.3, 0.5$. It is evident from these plots that an

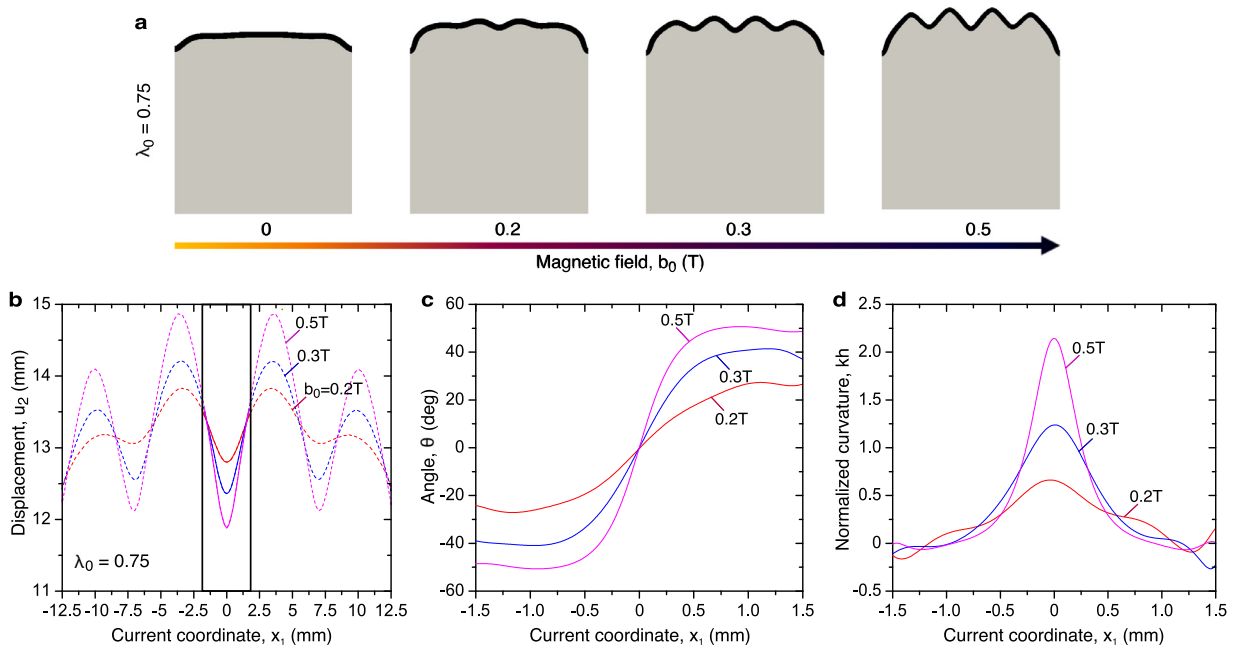

Fig. 10. Numerical results. (a) Morphological patterns for increasing magnetic field b_0 at $\lambda_0 = 0.75$. (b) Evolution of the displacement u_2 at the top surface of the MRE film at various applied magnetic fields b_0 as a function of the current coordinate x_1. (c) Evolution of the shear angle $\theta = \tan^{-1}(\partial u_2/\partial x_1)$ measuring the shearing of the faces of the central wrinkle-crinkle as a function of the current coordinate x_1. (d) Normalized curvature kh ($h = h_f$ the film thickness) of the central wrinkle-crinkle as a function of the current coordinate x_1.

initial wrinkled pattern for $b_0 = 0.3$ evolves gradually to sharper undulations for $b_0 = 0.5$. We focus on the middle crinkle and perform a quantitative study of the top film profile by analyzing the normal displacement u_2 shown in Fig. 10b at different applied fields b_0. From the u_2 profile, one can compute the shearing of the side facet of the crinkle via the shear angle, $\theta = \tan^{-1}(\partial u_2/\partial x_1)$, as well as the normalized curvature kh (with $h = h_f$ denoting the thickness of the film). In very close agreement with the corresponding experimental measurements in Fig. 3c,d, we obtain numerically an increasing shearing of the side facets of the crinkle with increasing b_0, which in turn leads to curvature localization in the mid point of the crinkle (see Fig. 10d). The values for θ and kh are in very good quantitative agreement with the experiments even though we make no attempt to compare them directly since it is evident that the numerical patterns overall are not identical with the corresponding experimental ones; for instance, for $\lambda_0 = 0.75$, we do not obtain a clear period-doubling, even though a weak asymmetry of the amplitude of the numerical wrinkles and crinkles is observed. A possible reason for those differences is the unfaithful modeling of the BVP itself since in the experiments the magnetic poles are set in a finite distance from the specimen, which even decreases with the development of the instability. In turn, the numerical BVP considers a large air domain and application of b_0 field far from it. Such effects will be analyzed in a future study. Even so in the present analysis, we capture qualitatively and fairly quantitatively the main features of the curvature lozalization.

This result allows us to use the numerical simulations to visualize the underlying local magnetic field distributions, which are not accessible in our experiments that mainly show the mechanical film profile and its spatial derivatives. Specifically, Fig. 11a-c shows the magnetic vector field at the top of the MRE film in consecutive zooms. In Fig. 11c, we observe that the opposite film facets are magnetized in the same directions creating effectively a large “magnetic” dipole response (depicted by the N-S vectors). These neighboring dipoles interact via the surrounding air and repel each other since they have the same direction of magnetization. This repulsion is, however, constrained by the neighboring magnetized crinkles as well as the film and substrate elasticity. This, in turn, leads to the strong shearing and elevation of the facets in the direction of the applied field.

This observation is quantified further in Figs. 11d-i, where we show the magnetic components m_1 and m_2 (and their in-plane derivatives with respect to x_1), respectively. In Fig. 11d, we observe that the perpendicular to the applied magnetic field b_0 component m_1 changes sign as one goes from $x_1 = -1.5$ to $x_1 = 1.5$ (where $x_1 = 0$ is set at the origin of the mid crinkle). The change of sign happens in a very localized region leading to magnetization localization as shown in Fig. 11f, similar to the curvature localization. In fact, we observe the creation of a rather sharp interface ($-0.4 \leq x_1 \leq 0.4$) in the perpendicular magnetic component m_1, which is otherwise fairly constant outside this regime. On the other hand, the normal component of the magnetization m_2 exhibits a reduction in that same interface region. Note that m_2 is substantially larger than m_1. As a result of this, the obtained interface allows to reduce the magnetic energy of the material (also known as demagnetization energy). The formation of this magnetic interface is, on the other hand, penalized by the elasticity of the film and the substrate, which does not allow for large curvature to be formed in that region. As a result, we can clearly identify

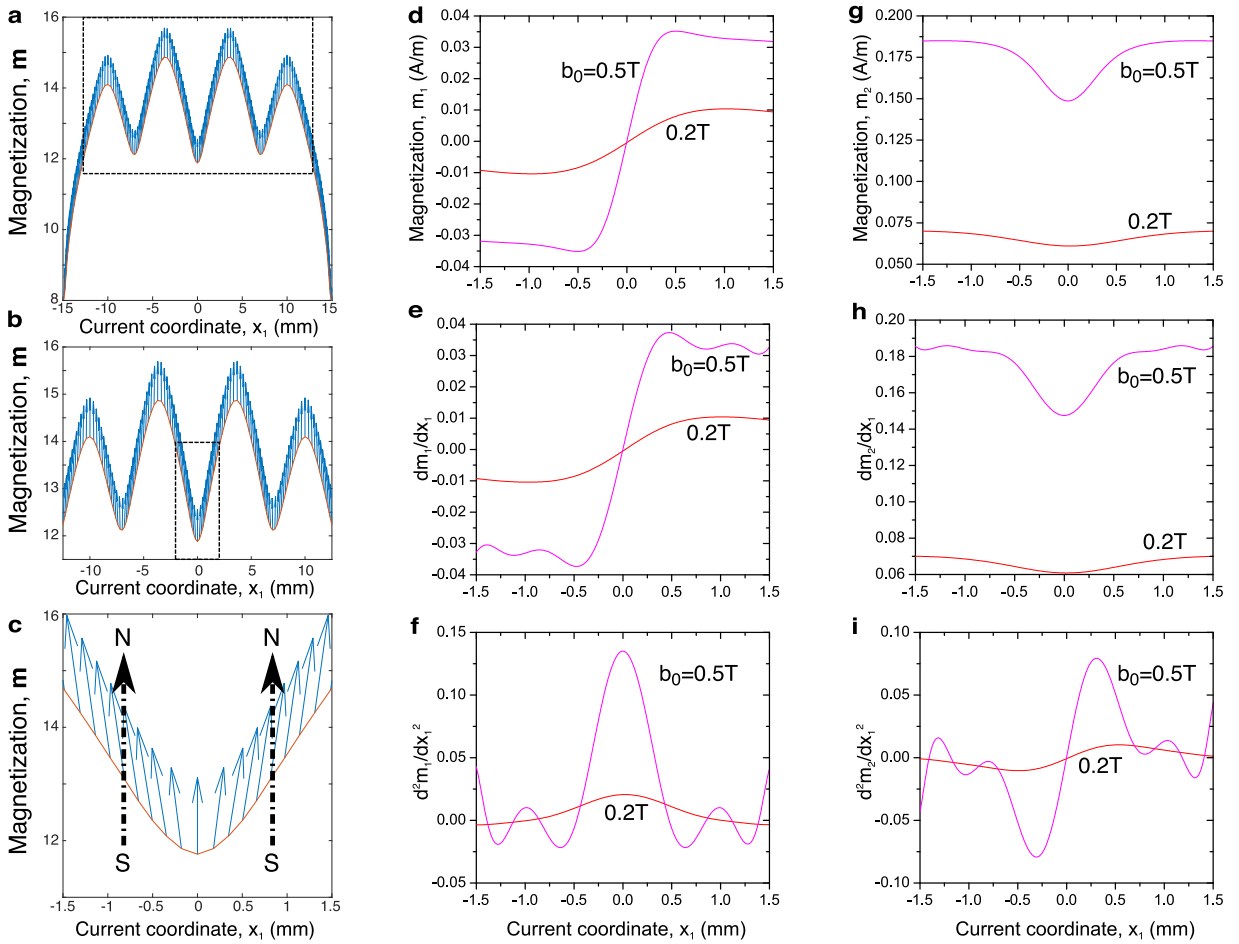

Fig. 11. (a-c) Numerical profiles and magnetization vector field of top surface of the MRE film. (c) The two opposite faces of the crinkled film repel each other due to their equal and coaxial overall magnetized response. (d-i) Analysis of the central crinkle. (d-f) Magnetization component m_1 and its first and second derivatives with respect to the current coordinate x_1. (f) Similar to curvature localization, magnetization localization of the transverse component m_1 is obtained in the crinkled region. (g-i) Magnetization component m_2 and its first and second derivatives with respect to the current coordinate x_1. Reduction of m_2 is observed in the central crinkled region.

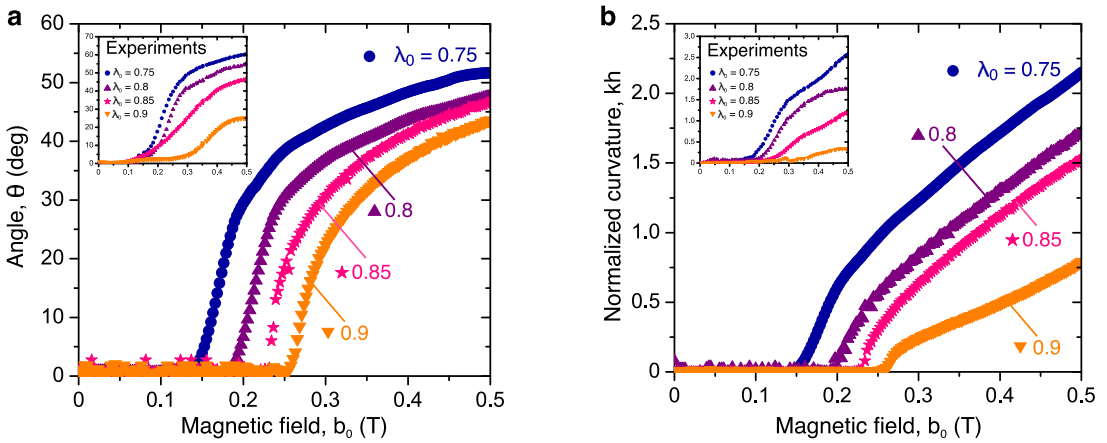

Fig. 12. Numerical evolution of (a) the shear angle θ and (b) the normalized curvature kh as a function of the applied magnetic field, b_0, and for various pre-compressions, $\lambda_0 = 0.75, 0.8, 0.85, 0.9$ at the central part of the film-substrate structure. Curvature localization appears in all pre-compressions considered here, $0.75 \leq \lambda_0 \leq 0.9$, albeit with decreasing amplitude for lower pre-compressions. All curves asymptote as a result of magnetic saturation. The insets show the corresponding experimentally obtained values of (**a**) θ and (**b**) kh. Good qualitative comparison is obtained between the experiments and the numerical estimates. Note the different axes values of the main and inset plots.

the competing mechanisms that lead to the creation of crinkles, i.e., the observation that the reduction of the magnetic energy leads to the simultaneous increase of the mechanical energy via the curvature localization. As a consequence, the relative importance of those two energies might or might not allow for such patterns to form depending on the geometry, constitutive response and boundary conditions. We should emphasize at this point that the same type of crinkles also appear in the numerical calculations without friction (see for instance the deformed shape for $f_c = 0$ in Fig. 7a). Nevertheless, the critical magnetic field at which they start developing depends naturally on the friction of the lateral faces.

In Fig. 12, we show that this crinkling formation is a universal feature in the sense that it is present for all applied pre-compressions. We demonstrate in this figure that both the shear angle and curvature localization are in good qualitative and even fair quantitative agreement with the corresponding experimental measures. Again, similar to the corresponding experimental data in Fig. 4b, we observe in Fig. 12b that the curvature localization curves increase from a zero value at magnetic fields that are higher than those obtained for the corresponding wrinkling bifurcation in Figs. 9a,b. This directly suggests that this departure point from zero in Fig. 12b may be used as a potential criterion to identify the onset of the secondary crinkle bifurcation.

Special note is needed for the case of small pre-compressions ($\lambda_0 \geq 0.9$), where the two-dimensional surface patterns found in the experiments (see inset of Fig. 1d) are not captured exactly by the present plane-strain FE simulations as discussed in the context of Fig. 8. Such work is underway and will be presented elsewhere.

5. Concluding Remarks

The present study investigates experimentally and numerically the stability and post-bifurcation of a magnetorheological elastomer (MRE) film bonded on a passive elastomer substrate. The film-substrate system is subjected to a combination of uniaxial mechanical pre-compression loads and transverse to the film magnetic fields. The purpose of this work is to analyze qualitatively and quantitatively the pattern formation and its evolution at large magnetic fields and pre-compressions.

The main observation of this study is the evolution of smooth wrinkle patterns (i.e., sinusoidal type surface formations) to crinkles which exhibit significant curvature and magnetization localization. The experimentally and numerically observed curvature localization is a direct consequence of the magnetic repulsion occurring at opposite facets of the crinkles coupled together with the necessity to minimize the demagnetization energy of the film. These magnetic effects are found to be in competition with the purely mechanical response of the film and the substrate, which in turn try to minimize the elastic energy and more particularly the curvature at the minimum and maximum points of the crinkled geometry.

Furthermore, the crinkled geometry may also be directly attributed to the very strong shearing in the opposite facets which in the present case is induced by the applied magnetic field. Nonetheless, such strong shearing has also been observed in the recent studies of graphene by Kothari et al. (2018) as well as in anisotropic hierarchical beams by Tarantino and Danas (2019). This, in turn, implies that such curvature localization can even occur in purely mechanical systems provided that they allow for significant shearing (such as anisotropic ones).

A second observation of the present study is the effect of the lateral friction to the observed pattern formation. As already discussed partially in Psarra et al. (2017), we find that increase of friction on the lateral surfaces is able to switch off the purely mechanical wrinkling instability but not the magneto-mechanical one. In that regime, we observe that the mechanical and magnetic modes do not interact strongly as a result of the switching off of the mechanical wrinkling. This leads to an asymptotic response of the critical magnetic field at large pre-compressions. In other words, the critical magnetic field required for magneto-mechanical wrinkling reduces with increasing pre-compression up to $\lambda_0 = 0.8$. But upon further pre-compression, the mechanical and magnetic load effects “decouple” as a result of the increasing effect of friction leading to no further decrease of the critical magnetic field.

In this view, the present analysis reveals the strong boundary effects that one can have in such a system. In practical terms, this can be partially resolved by reducing the thickness of the film, which leads to the increase of the number of wrinkles along the length of the specimen and hence reduces the effect of lateral friction upon the pattern formation. This, in turn, could lead to even lower critical magnetic fields upon increase of applied pre-compression in agreement with the frictionless numerical results shown in the present study and the theoretical analysis of Danas and Triantafyllidis (2014). Such an effort is underway and will be presented in a future study. In addition, one can think of disposing of the pre-compression device by pre-stretching the underlying substrate and then depositing the film. Such an approach, however, would at one hand necessitate to introduce an anisotropic response of the substrate (Cai and Fu, 2019), while at the same time would negate the advantage of using a single active device to create different patterns by adjusting in real time both the magnetic field and the pre-compression.

In addition, it is important to mention that in the present study, we have used two main simplifications. The first is related to the simple magneto-mechanical energy function proposed to describe the response of the MRE film. While this energy function is sufficiently rich to recover the wrinkling and crinkling modes, quantitatively, it becomes less accurate when strong magnetostrictive strains are developed in the crinkled faces. For a better accuracy, one needs to resort to more elaborate magneto-mechanical models such as the one proposed recently by Lefèvre et al. (2017). This model would also allow for a seamless wide parametric study of the effect of particle volume fraction and material stiffness upon the critical magnetic fields and patterns. The second simplification of the present study is the use of a large air domain and an applied magnetic field far from the specimen. Such a geometry assumes a homogeneously applied background Eulerian magnetic field that remains unperturbed far from the specimen. The actual experiment instead involves the presence of two magnetic

poles at finite distance from the MRE film, which deep in the post-bifurcation regime tend also to attract the film surface. Both of these simplifications can be substantially improved and such work is underway.

The idea of combining mechanical and magnetic or electric loads to obtain a variety of patterns can be applied in a number of other materials such as electro-active polymers (Wang et al., 2014b), liquid crystal elastomers (Danas et al., 2019; Wang et al., 2014a) and the recently proposed h-MREs (Kim et al., 2018). On the other hand, one can also use different geometries such as the ones discussed in Bertoldi et al. (2010), Tipton et al. (2012) and Danas (2017), where the rotation of ellipsoidal meso-structures can lead to negative and positive swelling as well as structures with an apparent in-plane negative Poisson ratio response. In addition, as already shown in the present study, the proposed MRE film-substrate systems can exhibit more complex two-dimensional patterns when biaxial or no pre-compression is applied. Such a study along the lines of its purely mechanical counterpart (Audoly and Boudaoud, 2008) are underway.

Acknowledgments

The authors would like to acknowledge support of the European Research Council (ERC) under the European Union's Horizon 2020 research and innovation program (grant agreement No 636903 - MAGNETO).

References

Abaqus, D.S., 2018. ABAQUS/Standard Version 2018, user manual. Simulia Corp.
Audoly, B., Boudaoud, A., 2008. Buckling of a stiff film bound to a compliant substrate–part i: Formulation, linear stability of cylindrical patterns, secondary bifurcations. J. Mech. Phys. Solids 56 (7), 2401–2421.
Auguste, A., Jin, L., Suo, Z., Hayward, R.C., 2017. Post-wrinkle bifurcations in elastic bilayers with modest contrast in modulus. Extr. Mech. Lett. 11, 30–36.
Bertoldi, K., Reis, P.M., Willshaw, S., Mullin, T., 2010. Negative Poisson's ratio behavior induced by an elastic instability. Adv Mater 22 (3), 361–366.
Bodelot, L., Voropaieff, J.-P., Pössinger, T., 2018. Experimental investigation of the coupled magneto-mechanical response in magnetorheological elastomers. Exp. Mech. 58 (2), 207–221.
Bowden, N., Brittain, S., Evans, A.G., Hutchinson, J.W., Whitesides, G.M., 1998. Spontaneous formation of ordered structures in thin films of metals supported on an elastomeric polymer. Nature 393, 146–149.
Bustamante, R., 2010. Transversely isotropic nonlinear magneto-active elastomers. Acta Mechanica 210 (3-4), 183–214.
Bustamante, R., Dorfmann, A., Ogden, R.W., 2008. On variational formulations in nonlinear magnetoelastostatics. Math. Mech. Solid 13, 725–745.
Cai, S., Breid, D., Crosby, A., Suo, Z., Hutchinson, J., 2011. Periodic patterns and energy states of buckled films on compliant substrates. J. Mech. Phys. Solids 59 (5), 1094–1114.
Cai, S., Chen, D., Suo, Z., Hayward, R.C., 2012. Creasing instability of elastomer films. Soft Matter 5, 1301–1304.
Cai, Z., Fu, Y., 2019. Effects of pre-stretch, compressibility and material constitution on the period-doubling secondary bifurcation of a film/substrate bilayer. Int. J. Non-Linear Mech. 115, 11–19.
Cao, C., Chan, H.F., Zang, J., Leong, K.W., Zhao, X., 2014. Harnessing localized ridges for high-aspect-ratio hierarchical patterns with dynamic tunability and multifunctionality. Adv. Mater. 26 (11), 1763–1770.
Cao, Y., Hutchinson, J.W., 2012. From wrinkles to creases in elastomers: the instability and imperfection-sensitivity of wrinkling. P. Roy. Soc. A-Math. Phy. 468 (2137), 94–115.
Danas, K., 2017. Effective response of classical, auxetic and chiral magnetoelastic materials by use of a new variational principle. J. Mech. Phys. Solids 105, 25–53.
Danas, K., Kankanala, S., Triantafyllidis, N., 2012. Experiments and modeling of iron-particle-filled magnetorheological elastomers. J. Mech. Phys. Solids 60 (1), 120–138.
Danas, K., Mukherjee, D., Haldar, K., Triantafyllidis, N., 2019. Bifurcation analysis of twisted liquid crystal bilayers. J. Mech. Phys. Solids 123, 61–79. The N.A. Fleck 60th Anniversary Volume
Danas, K., Triantafyllidis, N., 2014. Instability of a magnetoelastic layer resting on a non-magnetic substrate. J. Mech. Phys. Solids 69, 67–83.
Diab, M., Zhang, T., Zhao, R., Gao, H., Kim, K.-S., 2013. Ruga mechanics of creasing: from instantaneous to setback creases. Proc. R. Soc. A 469 (2157), 20120753.
Dorfmann, A., Ogden, R.W., 2003. Magnetoelastic modelling of elastomers. Eur. J. Mech. A/Solids 22 (4), 497–507.
Dorfmann, A., Ogden, R.W., 2005. Some problems in nonlinear magnetoelasticity. Zeitschrift für angewandte Mathematik und Physik ZAMP 56 (4), 718–745.
Galipeau, E., Ponte Castañeda, P., 2013. A finite-strain constitutive model for magnetorheological elastomers: Magnetic torques and fiber rotations. J. Mech. Phys. Solids. 61 (4), 1065–1090.
Huang, R., 2005. Kinetic wrinkling of an elastic film on a viscoelastic substrate. J. Mech. Phys. Solids 53 (1), 63–89.
Huck, W.T.S., Bowden, N., Onck, P., Pardoen, T., Hutchinson, J.W., Whitesides, G.M., 2000. Ordering of spontaneously formed buckles on planar surfaces. Langmuir 16, 3497–3501.
Hutchinson, J.W., 2013. The role of nonlinear substrate elasticity in the wrinkling of thin films. Phil. Trans. Royal Soc. A 371, 0422.
Jin, L., Suo, Z., 2015. Smoothening creases on surfaces of strain-stiffening materials. J. Mech. Phys. Solids 74, 68–79.
Kalina, K.A., Brummund, J., Metsch, P., Kästner, M., Borin, D.Y., Linke, J.M., Odenbach, S., 2017. Modeling of magnetic hystereses in soft mres filled with ndfeb particles. Smart Mater. Struct. 26 (10), 105019.
Kankanala, S.V., 2007. On Finitely Strained Magnetoelastic Solids. Doctoral Dissertation, The University of Michigan, Ann Arbor.
Keip, M.-A., Sridhar, A., 2019. A variationally consistent phase-field approach for micro-magnetic domain evolution at finite deformations. J. Mech. Phys. Solid 125, 805–824.
Kim, P., Abkarian, M., Stone, H.A., 2011. Hierarchical folding of elastic membranes under biaxial compressive stress. Nat. Mater 10, 952–957.
Kim, Y., Yuk, H., Zhao, R., Chester, S.A., Zhao, X., 2018. Printing ferromagnetic domains for untethered fast-transforming soft materials. Nature 558 (7709), 274–279.
Kothari, M., Cha, M.-H., Kim, K.-S., 2018. Critical curvature localization in graphene. I. quantum-flexoelectricity effect. Proc. R. Soc. A 474 (2214), 20180054.
Kothari, M., Cha, M.-H., Lefevre, V., Kim, K.-S., 2019. Critical curvature localization in graphene. II. non-local flexoelectricity–dielectricity coupling. Proc. R. Soc. A 475 (2221), 20180671.
Lacour, S., Jones, J., Suo, Z., Wagner, S., 2004. Design and performance of thin metal film interconnects for skin-like electronic circuits. IEEE Electron Device Lett. 25 (4), 179–181.
Lefèvre, V., Danas, K., Lopez-Pamies, O., 2017. A general result for the magnetoelastic response of isotropic suspensions of iron and ferrofluid particles in rubber, with applications to spherical and cylindrical specimens. J. Mech. Phys. Solids 107, 343–364.
Li, R., Kothari, M., Landauer, A.K., Cha, M.-H., Kwon, H., Kim, K.-S., 2018. A new subcritical nanostructure of graphene crinkle-ruga structure and its novel properties. MRS Adv. 3 (45-46), 2763–2769.
Moon, F., Pao, Y., 1969. Vibration and dynamic instability of a beam-plate in a transverse magnetic field. J. Appl. Mech. 36 (1), 92–100.
Mukherjee, D., Danas, K., 2019. An evolving switching surface model for ferromagnetic hysteresis. J. Appl. Phys. 125 (3), 033902.

Pocivavsek, L., Dellsy, R., Kern, A., Johnson, S., Lin, B., Lee, K.Y.C., Cerda, E., 2008. Stress and fold localization in thin elastic membranes. Science 320 (5878), 912–916.
Ponte Castañeda, P., Galipeau, E., 2011. Homogenization-based constitutive models for magnetorheological elastomers at finite strain. J. Mech. Phys. Solids 59 (2), 194–215.
Psarra, E., Bodelot, L., Danas, K., 2017. Two-field surface pattern control via marginally stable magnetorheological elastomers. Soft. Matter 13, 6576–6584.
Schümann, M., Borin, D., Huang, S., Auernhammer, G., Müller, R., Odenbach, S., 2017. A characterisation of the magnetically induced movement of ndfeb–particles in magnetorheological elastomers. Smart Mater. Struct. 26 (9), 095018.
Stoop, N., Lagrange, R., Terwagne, D., Reis, P.M., Dunkel, J., 2015. Curvature-induced symmetry breaking determines elastic surface patterns. Nat. Mater. 14 (3), 337–342.
Sun, J.-Y., Xia, S., Moon, M.-W., Oh, K.H., Kim, K.-S., 2012. Folding wrinkles of a thin stiff layer on a soft substrate. Proc. Royal Soc. A 468, 932–953.
Tarantino, M., Danas, K., 2019. Programmable higher-order euler buckling modes in hierarchical beams. Int. J. Solid. Struct. 167, 170–183.
Taylor, R.L., 2011. FEAP - Finite Element Analysis Program.
Tipton, C.R., Han, E., Mullin, T., 2012. Magneto-elastic buckling of a soft cellular solid. Soft Matter 8, 6880–6883.
Wang, M., He, L., Zorba, S., Yin, Y., 2014. Magnetically actuated liquid crystals. Nano Lett. 14 (7), 3966–3971.
Wang, Q., Robinson, D., Zhao, X., 2014. On-demand hierarchical patterning with electric fields. Appl. Phys. Lett. 104 (23), 231–238.
Wang, Q., Zhao, X., 2013. Phase diagrams of instabilities in compressed film-substrate systems. J. App. Mech. 81 (5), 051004.
Zhao, R., Kim, Y., Chester, S.A., Sharma, P., Zhao, X., 2019. Mechanics of hard-magnetic soft materials. J. Mech. Phys. Solid. 124, 244–263.